

The present work was submitted to the Physics Institute IIIb

Modeling of the Optical Setting for the Measurement of the Electric Dipole Moment of Protons at Cooler Synchrotron COSY

Master Thesis

by

Mariia Manerova

Univ.-Prof. Dr. rer. nat. Andreas Lehrach

Univ.-Prof. Dr. rer. nat. Jörg Pretz

Aachen, October 2022

Abstract

Electric Dipole Moments (EDMs) of elementary particles are considered to be an excellent probe of physics beyond the Standard Model. They violate parity and time reversal, while through the CPT -theorem also breaking the CP -symmetry. The asymmetry of matter and antimatter in the Universe is not explained to a sufficient extent within the Standard Model (SM), requiring in turn additional sources of violation beyond it, which may manifest in the EDMs. A measurement of an EDM with the currently achievable precision would therefore be a strong indication for physics beyond the SM. The Jülich Electric Dipole moment Investigations (JEDI) collaboration aims to use storage rings to measure the permanent EDMs of protons and deuterons with high precision. Due to this, a dedicated electrostatic storage ring is currently under development. As an intermediate step, experiments are being conducted at an existing magnetic storage ring, the Cooler Synchrotron COSY in Jülich. One important prerequisite for these experiments is modeling of the optical settings and the beam orbit in COSY to analyze the EDM measurement results. This master thesis investigates the effects influencing the closed orbit and focuses on the model calculation of the beam orbit and optical functions of COSY. The results of a matching procedure, which helps to achieve a much better model description of COSY's orbit, are presented.

Contents

1	Introduction	1
2	Motivation	3
2.1	Matter-Antimatter Asymmetry	3
2.2	Electric Dipole Moment	4
3	Beam and Spin Dynamics in Storage Rings	6
3.1	Coordinate System	6
3.2	Transverse Beam Dynamics	7
3.2.1	Equations of Motion	7
3.2.2	Bending Magnets	11
3.2.3	Focusing Magnets	11
3.3	Dispersion and Chromaticity	13
3.4	Beam Position Monitors	16
3.5	Longitudinal Particle Motion	17
3.6	Spin Dynamics	20
3.6.1	Spin Formalism	20
3.6.2	Spin Motion	21
3.7	Electric Dipole Moment Searches in Storage Rings	22
4	Cooler Synchrotron COSY	25
4.1	Simulation Model	26
4.1.1	Implementation into the Bmad Code	27
4.1.2	Benchmarking of Particle Motion	28
4.2	Magnet Misalignments	32
4.3	Dipole Shortening	34
5	Model Fitting and Data Analysis	38
5.1	Orbit Correction	39

5.1.1	Orbit Response Matrix Calculation	40
5.2	Orbit Matching Procedure	41
5.2.1	Singular Value Decomposition	42
5.3	Analysis of the Simulation Results	42
6	Conclusion and Outlook	51
	Bibliography	53
A	Phase Space Simulations	61
B	Magnet Misalignments	62
C	Results of Model Fitting	65

1 Introduction

As of today, the reason why the observable Universe is composed solely of matter is unknown, and so far there is no information on where antimatter is preserved. In 1967, Andrei Sakharov [1] proposed his theory of the possible origin of such asymmetry. His theory today is known as Sakharov conditions. Violation of \mathcal{CP} -symmetry is one of those prerequisites. In spite of the fact that the Standard Model (SM) of particle physics implies the existence of this asymmetry, its magnitude is extremely small in comparison to the \mathcal{CP} -violation necessary to explain the excess of matter in the Universe [2]. An additional source of \mathcal{CP} -violation beyond the Standard Model could be the Electric Dipole Moments (EDMs) of elementary particles.

The search for permanent EDMs has been going on for about 60 years. The first experiments were conducted in neutral particle systems, and currently, measurements of the EDMs of charged particles, like protons and deuterons, are ongoing. The Jülich Electric Dipole moment Investigations (JEDI) collaboration aims to measure the EDM of both particles directly using the storage ring COSY (Cooler Synchrotron facility) in Forschungszentrum Jülich. As part of feasibility studies, since 2012 [3] the spin coherence time (SCT) of a deuteron has been measured. In 2016, Guidoboni et al. [4] presented the lengthened SCT of 1000 s measured at COSY. This was followed by two successful runs with deuterons in December 2018 and March 2021 [5].

The same achievements are anticipated for experiments with polarized protons. The first run for measurement and optimization of the spin coherence time of protons ended in March 2022.

Among the important tasks before conducting such experiments are the study of the experimental requirements as well as the accurate modeling of the real machine. The purpose of this thesis is to improve the COSY simulation model used for EDM experiments. The model incorporates all real effects influencing the closed orbit in the storage ring. Thus, the precise description of a facility is intended to further support the data analysis and the studying of the systematic effects. The model used in this thesis is based on the Bmad [6] software library. This work is roughly divided into theoretical and practical parts. The theoretical part cov-

ers topics such as general motivation for conducting EDM experiments, touching upon the problem of baryonic asymmetry (Section 2.1), and describing the concept of EDM (Section 2.2) itself.

Section 3 contains theoretical aspects of the beam and spin dynamics in the storage rings, describing the coordinate system used as well as introducing the equations of motion and the main magnets of the setup.

Section 4 concentrates directly on the COSY synchrotron facility itself. In addition to the general technical characteristics of the plant, the section describes its simulation model, as well as the systematic effects that influence the closed orbit, such as magnet misalignments and effective dipole length.

Section 5 refers to the practical part of the thesis, which concerns model fitting and data analysis. At this stage, the model includes all previously presented systematic effects in the storage ring. The first subsection highlights the aspect of orbit correction, also presenting the orbit response matrix (ORM) calculated for the actual magnet settings. Subsection 5.2 describes the algorithm that allows fitting the simulation model to a real orbit. And the final subsection presents the relevant calculations and simulation results for further experiments with the polarized protons.

In the final Section 6 the results are summarized and an outlook is given.

2 Motivation

2.1 Matter-Antimatter Asymmetry

As far as we know, our Universe is entirely made up of matter. This statement alone raises the question of where all the antimatter, created as a result of the Big Bang, has gone. Cosmology and the Standard Model of particle physics fail to explain this matter-antimatter-asymmetry. This asymmetry, also known as baryon-antibaryon-asymmetry, is expressed as a baryon-to-photon density ratio [7]:

$$\eta = \frac{n_B - n_{\bar{B}}}{n_\gamma}, \quad (2.1)$$

where n_B is the baryon density, $n_{\bar{B}}$ is the antibaryon density and n_γ is the photon density. This asymmetry was determined experimentally by two independent astrophysical observations. One is the analysis of the cosmic microwave background (CMB), and the second study was to determine the abundance of new nuclei of light elements, which were created during the Big Bang Nucleosynthesis (BBN). Both data show a good agreement [8], [9]:

$$\begin{aligned} \eta &= (6.07 \pm 0.33) \cdot 10^{-10} \quad (\text{BBN}) \\ \eta &= (6.16 \pm 0.06) \cdot 10^{-10} \quad (\text{CMB}) \end{aligned} \quad (2.2)$$

On the other hand the Standard Model of particle physics predicts the asymmetry to be eight orders of magnitude below the observed ratio $n_B/n_\gamma = n_{\bar{B}}/n_\gamma \simeq 10^{-18}$ [10].

This inconsistency can be explained by the fact that either we do not see the antimatter, because it accumulates out of our sight, or the annihilation itself occurred asymmetrically, leaving some of the matter in the universe. Such a process is known as baryogenesis.

Andrei Sakharov [1] formulated three conditions that should be met for baryogenesis to take place:

1. Baryon number violating process is needed to reach a state with an exceeding number of baryons over antibaryons.
2. \mathcal{C} and \mathcal{CP} violation, which distinguish the production rates of baryons and antibaryons.
3. The baryon generation has to take place outside of thermal equilibrium so that no inverse process occurs.

\mathcal{CP} -violating processes are included in the Standard Model so that the baryon number violation can be explained within its framework. However, the strength of these processes is too small to explain the baryon-antibaryon-asymmetry. Given that, it is appropriate to search for new sources of the \mathcal{CP} -violation beyond the Standard Model. The permanent electric dipole moment of an elementary particle appears to be one of the possible candidates.

2.2 Electric Dipole Moment

Electric dipole moment (EDM) \vec{d} is defined in terms of the electric charge density ρ as a permanent separation of charges inside a particle [11]:

$$\vec{d} = \int_V \rho(\vec{x}) \vec{x} d\vec{x}. \quad (2.3)$$

Equation (2.3) has a similar structure as the one, which describes the magnetic dipole moment (MDM) $\vec{\mu}$:

$$\vec{\mu} = \frac{1}{2} \int_V (\vec{x} \times \vec{j}(\vec{x})) d\vec{x}, \quad (2.4)$$

where $\vec{j}(\vec{x})$ is a current density. Both, EDM and MDM, are fundamental properties of a particle and have to be either parallel or anti-parallel to its spin \vec{S} [11]:

$$\begin{aligned} \vec{d} &= \eta \frac{q}{2mc} \vec{S} \\ \vec{\mu} &= g \frac{q}{2mc} \vec{S}, \end{aligned} \quad (2.5)$$

which includes the charge of the particle q , its mass m , and the speed of light c . The parameters \vec{d} and $\vec{\mu}$ are dimensionless quantities standing for EDM and MDM, respectively.

Consider a particle at rest with magnetic and electric dipole moments in external magnetic \vec{B} and electric \vec{E} fields. The corresponding Hamiltonian of such a particle is given by [2]:

$$H = -\vec{\mu}\vec{B} - \vec{d}\vec{E}. \quad (2.6)$$

Applying the parity \mathcal{P} and time reversal \mathcal{T} transformation, it can be seen that the Hamiltonian changes in both cases:

$$\begin{aligned} \mathcal{P} : H &= -\vec{\mu}\vec{B} - \vec{d}\vec{E} \rightarrow H = -\vec{\mu}\vec{B} + \vec{d}\vec{E} \\ \mathcal{T} : H &= -\vec{\mu}\vec{B} - \vec{d}\vec{E} \rightarrow H = -\vec{\mu}\vec{B} + \vec{d}\vec{E} \end{aligned} \quad (2.7)$$

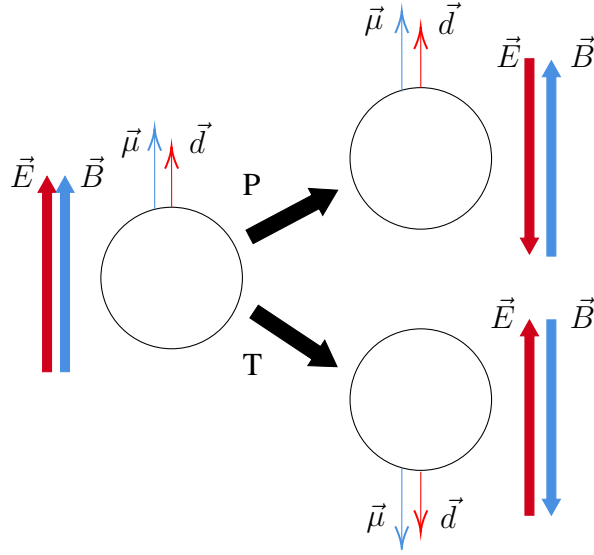


Figure 1: Behaviour of the EDM and MDM under parity \mathcal{P} and time reversal \mathcal{T} transformations. Applying a parity transformation flips the sign of the electric field \vec{E} , while time reversal transformation flips \vec{d} , $\vec{\mu}$, and the sign of the magnetic field \vec{B} . Adapted from [13].

Parity transformation inverts \vec{E} , which indicates that \mathcal{P} -symmetry is violated. Applying the \mathcal{T} -transformation also changed the sign of \vec{B} , which implies a violation of time reversal symmetry [12]. This is illustrated in Figure 1. Violation of both, \mathcal{P} and \mathcal{T} symmetries under assumption that \mathcal{CPT} symmetry is conserved, directly implies the \mathcal{CP} -violation [7].

Up to date, only the upper bounds on EDMs were found and not the EDMs themselves. Moreover, determining the EDM of one of the particles will not provide any information about the source of the \mathcal{CP} - violation, therefore it is required to measure the EDM for various particles [14]. Table 1 summarizes the current EDM limits.

Particle	Upper limit
Neutron	$1.8 \cdot 10^{-26}$ e cm (90% C.L.) [15]
Electron	$8.7 \cdot 10^{-29}$ e cm (90% C.L.) [16]
Proton	$7.9 \cdot 10^{-25}$ e cm (95% C.L.) [17]

Table 1: Measured upper limits of EDM searches.

3 Beam and Spin Dynamics in Storage Rings

The knowledge of beam and spin dynamics is a fundamental requirement for studying the nature of the EDM of a particle in a storage ring. In this chapter the mathematical tools employed to describe the particle motion, including the coordinate system and the magnetic elements used in the accelerator are discussed.

3.1 Coordinate System

As it was mentioned before, in order to describe the trajectory of the particles in the accelerator, it is necessary to define a coordinate system. When studying beam dynamics, it is crucial to determine the deviations from a specified reference orbit for all particles. For this purpose, a reference particle is defined. It follows exactly the design and/or reference orbit \vec{r}_{ref} with the reference momentum \vec{p}_{ref} of the beam. The second step, to describe the motion of an individual particle, requires the introduction of a co-moving orthogonal coordinate system $(\vec{e}_x, \vec{e}_y, \vec{e}_z)$ [18], whose origin follows the reference particle. Figure 2 demonstrates such a coordinate system, showing the movement of a particle on the reference orbit from its initial position to the final.

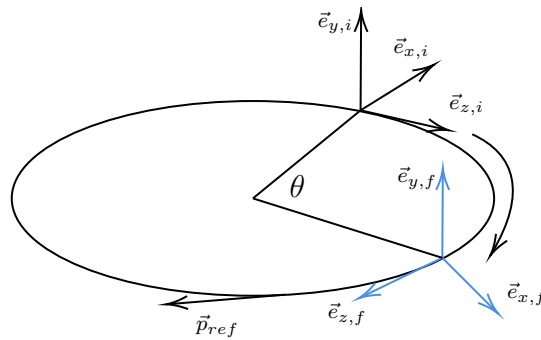


Figure 2: Co-moving Cartesian coordinate system $(\vec{e}_x, \vec{e}_y, \vec{e}_z)$ with its origin located at the position of reference particles. The initial position of a particle is depicted in black and the final position is in blue, whereas θ is an angle between them.

In Figure 2 the vector \vec{e}_z is aligned with the momentum vector \vec{p}_{ref} of a reference particle, while the unit vectors \vec{e}_x and \vec{e}_y span the transverse plane orthogonal to \vec{e}_z . The transforma-

tion of the unit vectors from the initial to the final position is given by [19]:

$$\begin{aligned}\vec{e}_{x,f} &= \cos(\theta) \cdot \vec{e}_{x,i} + \sin(\theta) \cdot \vec{e}_{z,i} \\ \vec{e}_{y,f} &= \vec{e}_{y,i} \\ \vec{e}_{z,f} &= -\sin(\theta) \cdot \vec{e}_{x,i} + \cos(\theta) \cdot \vec{e}_{z,i},\end{aligned}\tag{3.1}$$

with

$$\theta = \int_i^f \frac{ds}{\rho(s)},\tag{3.2}$$

where $\rho(s)$ is a bending radius [19].

The particle trajectory is now given by:

$$\vec{r}(s) = \vec{r}_{ref}(s) + x(s)\vec{e}_x(s) + y(s)\vec{e}_y(s),\tag{3.3}$$

where $x(s)$ and $y(s)$ describe transverse deviations from the reference orbit of a single particle [20].

3.2 Transverse Beam Dynamics

Transverse motion in an accelerator refers to a particle movement under the influence of the external transverse bending and focusing [21]. Here, the phase space is given by a plane spanned between horizontal and vertical coordinates. The equations of motion in this plane, as well as the magnetic structure of the accelerator and its effect on the beam trajectory, are discussed further in this section.

3.2.1 Equations of Motion

Equation (3.3) represents a general form of the position vector $\vec{r}(s)$ of a particle. To formulate the equations of motion, first and second-order time derivatives of the position vector are needed [19]:

$$\begin{aligned}\dot{\vec{r}}(s) &= \dot{x}\vec{e}_x + \dot{y}\vec{e}_y + \left(1 + \frac{x}{\rho}\right) \dot{s}\vec{e}_z, \\ \ddot{\vec{r}}(s) &= \left[\ddot{x} - \left(1 + \frac{x}{\rho}\right) \frac{\dot{s}^2}{\rho}\right] \vec{e}_x + \ddot{y}\vec{e}_y + \left[\frac{2}{\rho}\dot{x}\dot{s} + \left(1 + \frac{x}{\rho}\right) \ddot{s}\right] \vec{e}_z,\end{aligned}\tag{3.4}$$

with

$$\begin{aligned}\dot{x} &= \frac{dx}{dz} \frac{dz}{dt} = x' \dot{s}, \\ \ddot{x} &= \dot{x}' \dot{s} + x'' \dot{s}^2 + x' \ddot{s}.\end{aligned}\tag{3.5}$$

A particle's position s is uniquely defined for any time t when it passes through the accelerator. As a result, the time derivative, \dot{x} , can be substituted with a derivative with respect to coordinate s [19], x' , which results into:

$$\dot{\vec{r}}(s) = x' \dot{s} \vec{e}_x + y' \dot{s} \vec{e}_y + \left(1 + \frac{x}{\rho}\right) \dot{s} \vec{e}_z, \quad (3.6)$$

$$\ddot{\vec{r}}(s) = \left[x'' \dot{s}^2 + x' \ddot{s} - \left(1 + \frac{x}{\rho}\right) \frac{\dot{s}^2}{\rho} \right] \vec{e}_x + (y'' \dot{s}^2 + y' \ddot{s}) \vec{e}_y + \left[\frac{2}{\rho} x' \dot{s}^2 + \left(1 + \frac{x}{\rho}\right) \ddot{s} \right] \vec{e}_z. \quad (3.7)$$

In the presence of electromagnetic fields, a particle motion can be expressed as:

$$F_L = \frac{d\vec{p}}{dt} = q(\vec{E} + \vec{v} \times \vec{B}), \quad (3.8)$$

where q is the electric charge, \vec{E} and \vec{B} are the electric and magnetic field respectively, and \vec{v} is a particle's velocity. Equation (3.8) represents the Lorentz force law [18]. For a particle traversing a pure magnetic accelerator, i.e. $\vec{B} = (B_x, B_y, 0)$, with momentum $\vec{p} = m\dot{\vec{r}}$ and velocity $\vec{v} = \dot{\vec{r}}$ Equation (3.8) reduces to

$$\ddot{\vec{r}}(s) = \frac{q}{m} (\dot{\vec{r}}(s) \times \vec{B}), \quad (3.9)$$

hence

$$\ddot{\vec{r}}(s) = \frac{q}{m} \begin{pmatrix} -(1 + \frac{x}{\rho}) \dot{s} B_y \\ (1 + \frac{x}{\rho}) \dot{s} B_x \\ x' \dot{s} B_y - y' \dot{s} B_x \end{pmatrix}. \quad (3.10)$$

Combining Equations (3.6), (3.7) and (3.10) results into:

$$\begin{aligned} x'' \dot{s}^2 + x' \ddot{s} - \left(1 + \frac{x}{\rho}\right) \frac{\dot{s}^2}{\rho} &= -\frac{q}{m} B_y \left(1 + \frac{x}{\rho}\right) \dot{s}, \\ y'' \dot{s}^2 + y' \ddot{s} &= \frac{q}{m} B_x \left(1 + \frac{x}{\rho}\right) \dot{s}. \end{aligned} \quad (3.11)$$

Assuming that the particles' velocity varies slowly while passing through the magnetic field, i.e. $\ddot{s} \approx 0$, and $v = \dot{s} \left(1 + \frac{x}{\rho}\right)$, Equations (3.11) yield [19]

$$x'' - \left(1 + \frac{x}{\rho}\right) \frac{1}{\rho} = -\frac{v}{\dot{s}} \frac{q}{p} B_y \left(1 + \frac{x}{\rho}\right), \quad (3.12)$$

$$y'' = \frac{v}{\dot{s}} \frac{q}{p} B_x \left(1 + \frac{x}{\rho}\right). \quad (3.13)$$

Therefore, for the particles with a momentum $p = p_0 + \Delta p$ deflected in a horizontal plane, with

$$\begin{aligned}\frac{q}{p_0} B_y &= \frac{1}{\rho} - kx, \\ \frac{q}{p_0} B_x &= \frac{1}{\rho} - kz,\end{aligned}\tag{3.14}$$

the equations of motion take the form:

$$x''(s) + \left(\frac{1}{\rho^2(s)} - k(s) \right) x(s) = \frac{1}{\rho(s)} \frac{\Delta p}{p_0}\tag{3.15}$$

$$y''(s) + k(s)y(s) = 0,\tag{3.16}$$

These equations are known as *Hill's differential equations* [22], [18].

Ignoring momentum deviations, i.e. $\frac{\Delta p}{p_0} = 0$, Equations (3.15), (3.16) get a form of second order homogeneous differential equations:

$$x''(s) + k(s)x(s) = 0\tag{3.17}$$

$$y''(s) + k(s)y(s) = 0.$$

Since Equations (3.17) have the same structure, consider the solution in the horizontal direction:

$$\begin{aligned}x(s) &= Au(s) \cos(\phi(s) + \phi_0), \\ x(s) &= \sqrt{\epsilon} \sqrt{\beta(s)} \cos(\phi(s) + \phi_0),\end{aligned}\tag{3.18}$$

where $\phi(s)$ represents a phase advance, ϕ_0 a phase, and the combination of the parameters $A^2 = \epsilon$ and $u^2(s) = \beta(s)$ gives an amplitude of an oscillation, with ϵ being an emittance and $\beta(s)$ a betatron function [18]. To characterize the beam an envelope $E(s)$ of a beam is defined [18]:

$$E(s) = \sqrt{\epsilon\beta(s)},\tag{3.19}$$

which is determined by the amplitude of betatron oscillations (Figure 3). One of the parameters – emittance ϵ – is a constant defining the size of a particle beam, while β -function is a quantity depending on a beam focusing [19]. Apart from that, the β -function is also linked to other optical functions α and γ [18], which can be derived for x and y phase space:

$$\alpha(s) = -\frac{d\beta(s)/ds}{2}\tag{3.20}$$

$$\gamma(s) = \frac{1 + \alpha^2(s)}{\beta(s)}.\tag{3.21}$$

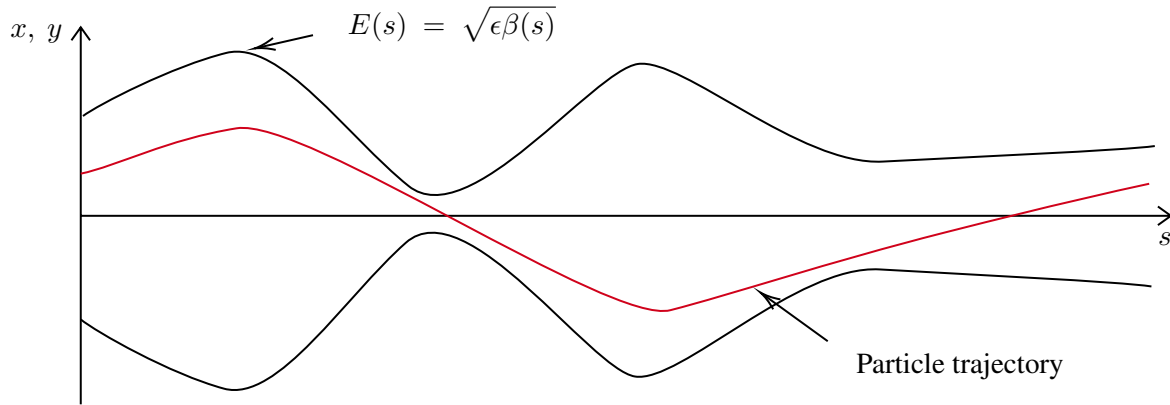


Figure 3: Particle trajectory within a beam envelope $E(s)$. Its size is determined by a particle with the highest emittance value ϵ . Adapted from [19].

These optical functions are used to describe an ellipse comprising all the beam particles in the phase space, resulting in:

$$\gamma(s)x^2(s) + 2\alpha(s)x(s)x'(s) + \beta(s)x'^2(s) = \epsilon. \quad (3.22)$$

This is a general equation of a phase space ellipse (Figure 4) with an enclosed area $A = \pi\epsilon$.

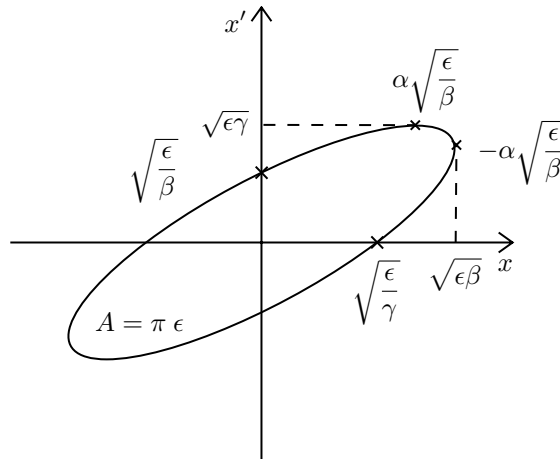


Figure 4: Phase space ellipse of particle motion for a horizontal phase space. The horizontal offset is given by a shift along the x -axis. The x' -axis gives a derivative of an offset. The optical functions α , γ , and β define the size and shape of an ellipse. The area of the ellipse A is defined by an emittance ϵ . Adapted from [19].

3.2.2 Bending Magnets

Typically, in circular accelerators, magnetic fields are used to bend and focus the particle beam. As shown in Equation (3.8), the Lorentz force acting on the particles combines both, electric and magnetic fields. However, for particles with high momenta, it is appropriate to exclude electric fields and only use magnetic fields to bend and focus the particle beams [23]. Hence, combining Lorentz and centrifugal forces for a perfectly circular orbit, the bending radius in bending dipoles is given by:

$$\frac{1}{\rho} = \frac{q}{p}B, \quad (3.23)$$

where $p = \gamma mv$ is a particle's momentum. Integrating over the curvature in the magnet results in a bending angle α [18]:

$$\alpha = \int \frac{ds}{\rho} = \int b \frac{q}{p} ds = \frac{q}{p}B \cdot l, \quad (3.24)$$

where l is a length of a magnet. Bending magnets, or dipoles, are the main components of the circular accelerator since they are used to bend the particle beam. There are also smaller dipole magnets mounted alongside the main dipoles, which are used to steer the beam, applying smaller kicks to correct the orbit to match the reference (see Section 5.2).

3.2.3 Focusing Magnets

The other key magnetic components in the accelerator are the quadrupoles. The schematic of a quadrupole is shown in Figure 5. These magnets focus the beam to keep the particles close together. Providing stability of transverse motion is possible with a carefully designed focusing structure, which in turn also helps to maintain the desired beam size in the ring [23]. Since the magnetic field produced by the quadrupoles is proportional to the distance from the magnet's center, it will behave similarly to how a lens does for light [18]. The deflection angle of a quadrupole is given by:

$$\theta = -\frac{l}{\rho} = -\frac{qc}{\beta E}Bl = -\frac{qc}{\beta E}grl, \quad (3.25)$$

where l is the length of the particle trajectory within a quadrupole with a magnetic field B , $g = \frac{\partial B}{\partial x}$ is a field gradient and E is the particle's energy.

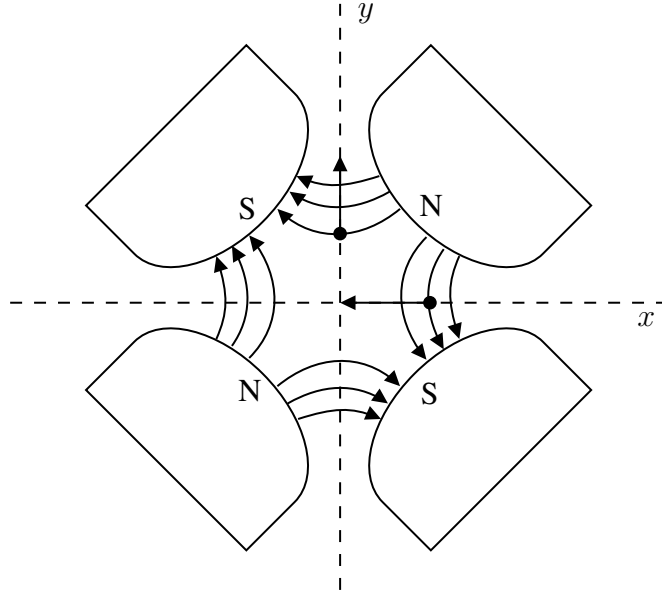


Figure 5: A schematic cross-section of a quadrupole magnet with magnetic field lines. The beam goes perpendicular to the x-y-plane. Adapted from [19].

Similarly to the bending radius the strength k of the focusing magnet can be expressed with [23]

$$k = \frac{q}{p}g. \quad (3.26)$$

This way, if the beam is shifted from the center horizontally, the quadrupole magnet deflects the particles, which leads to a focusing effect. But at the same time, the trajectories of particles that are vertically offset will be bent outward and defocused [19]. Thus, quadrupoles focusing in one particular direction, are defocusing in another. In Hill's equations (3.15), (3.16) such a property is represented by a sign of a quadrupole strength k , e.g. a quadrupole defocusing in a vertical direction has a negative value of k .

To get a focusing effect in both planes, it is necessary to implement a combination of focusing and defocusing magnets. This combination keeps the particles inside the accelerator but causes them to oscillate around an ideal orbit. This oscillation is called a betatron oscillation [18]. The number of betatron oscillations per revolution is called a betatron tune. It is related to the total phase advance $\phi(s) = \frac{1}{2\pi} \int_0^s \frac{1}{\beta(\hat{s}')} d\hat{s}'$ as [24]:

$$Q_i = \frac{1}{2\pi} \oint \frac{ds}{\beta_i(s)}. \quad (3.27)$$

3.3 Dispersion and Chromaticity

Dispersion is an intrinsic property of dipole magnets and cannot be ruled out. Therefore, the orbit on which the particle moves should be considered as a sum of the desired orbit and dispersion. This disturbed orbit is also affected by the focusing force of other magnets in the accelerator.

As shown in Equation (3.15) the particle's horizontal motion is effected by a momentum deviation $\frac{\Delta p}{p_0}$. Consider a particle traveling through a dipole in the absence of a quadrupole field [18]:

$$x''(s) + \frac{1}{\rho^2(s)}x(s) = \frac{1}{\rho(s)}\frac{\Delta p}{p_0}. \quad (3.28)$$

The resulting equation is an inhomogeneous differential equation, which general solution $x_g(s)$ includes a homogeneous $x_\beta(s)$ and an inhomogeneous part $x_i(s)$ [25]. The homogeneous solution describes the betatron oscillation, while the inhomogeneous part represents an additional contribution to the motion due to momentum deviation [18], [20]:

$$x_g(s) = x_\beta(s) + x_i(s) = x_\beta(s) + D(s)\frac{\Delta p}{p_0}, \quad (3.29)$$

where $D(s)$ is *dispersion*.

As the dispersion results from a mismatch in the bending power of the dipoles in presence of momentum, it is directly related to the curvature $\rho(s)$. A similar effect occurs at the quadrupoles. When compared to a particle with a reference momentum, particles with a momentum deviation from p_0 are exposed to a different quadrupole strength, which causes them to focus differently. The effect is shown in Figure 6. The quadrupole strength experienced by a particle with momentum $p = p_0 + \Delta p$, assuming only minor deviations from the reference momentum, is given by [25]:

$$k(p) = -\frac{q}{p}g = -\frac{q}{p_0 + \Delta p}g \approx -\frac{q}{p_0}\left(1 - \frac{\Delta p}{p_0}\right)g = k_0 - \Delta k. \quad (3.30)$$

Hence, momentum deviation can be interpreted as a quadrupole strength error [19]:

$$\Delta k = \frac{\Delta p}{p_0}k_0 \quad (3.31)$$

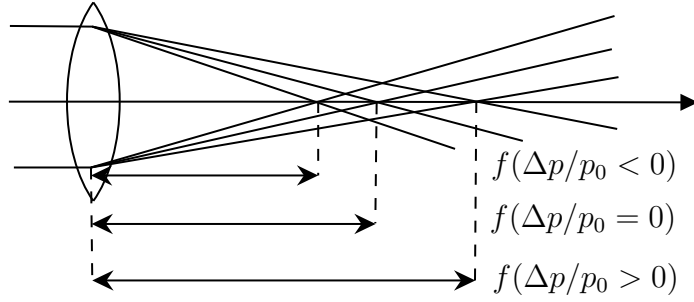


Figure 6: Chromatic focusing errors caused by the variation of the focal length f of the quadrupole. This effect of momentum dependence is called chromaticity. The focusing quadrupole is represented by a focusing lens. Adapted from [18].

Such a quadrupole error leads to a change in the betatron tune over a distance ds [19] followed by a tune shift, calculated by integrating over all quadrupoles:

$$\begin{aligned} dQ &= \frac{\Delta p}{p_0} \frac{1}{4\pi} k_0 \beta(s) ds, \\ \Delta Q &= \frac{1}{4\pi} \oint k_0 \cdot \beta(s) ds. \end{aligned} \quad (3.32)$$

Hence, the resulting dimensionless quantity

$$\xi := \frac{\Delta Q}{\Delta p/p_0} = \frac{1}{4\pi} \oint k(s) \beta(s) ds \quad (3.33)$$

is called natural *chromaticity*. Quadrupoles with high focusing strength and a significant betatron function provide the majority of the contributions. It is necessary to account for chromaticity since a tune shift may result in a shift of a working point of offset particles at optical resonances [18] and a subsequent particle loss. At positions with non-vanishing dispersion, a chromaticity correction is carried out. For this purpose, sextupole magnets with focusing strengths depending on transverse position are installed there. Hence, the ring's final chromaticity is a result of the quadrupoles' induction of the ring's natural chromaticity and the sextupoles' chromaticity correction. The concept of chromaticity compensation using sextupoles is schematically depicted in Figure 7. The sextupoles generate a non-linear field along the x-axis which can be described by:

$$G_z(x) = \frac{1}{2} g' x^2, \quad (3.34)$$

with the second derivative of a vertical component $\frac{d^2 G_z(s)}{dx^2} = g'$ defining the coupling of horizontal and vertical particle motion inside the magnet [19].

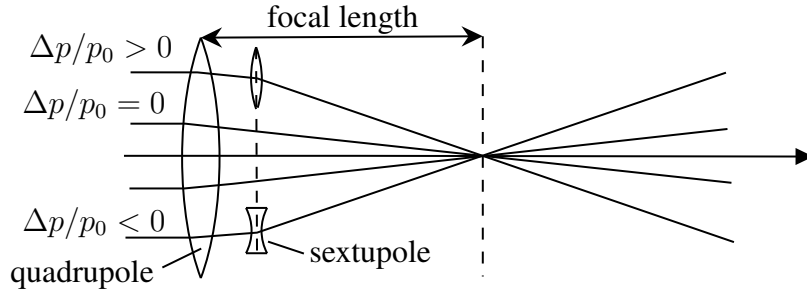


Figure 7: Chromaticity correction with sextupoles. Particles of higher energy are focused less and particles of lower energy than an ideal particle are focused more by a sextupole. Adapted from [18].

A sextupole consists of six magnet poles defining an arrangement of alternating polarity (see Figure 8). The sextupole field strength along the beam axis is given by [19]:

$$m = \frac{q}{p} g' = \frac{q}{p} 6\mu_0 \frac{nI}{a^3}, \quad (3.35)$$

where n is the number of coils, I is a coil current, and a is a pole radius.

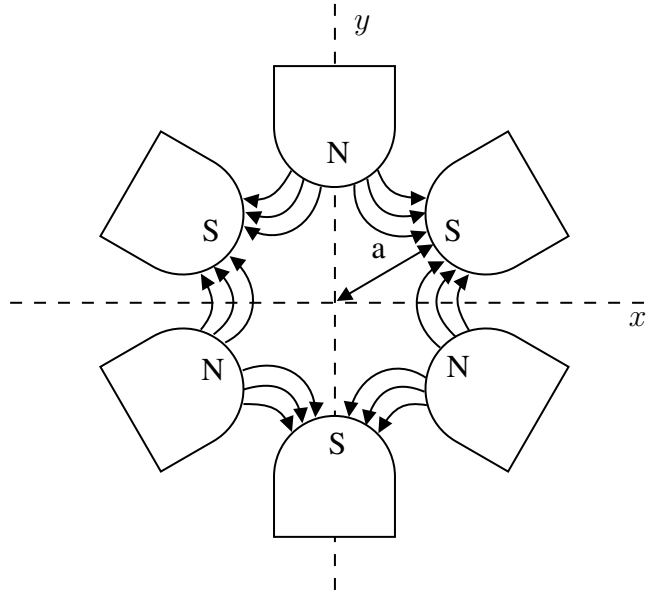


Figure 8: Schematic of a sextupole magnet with poles and equipotential lines. a is the distance from the center of a magnet to the pole. Adapted from [19].

3.4 Beam Position Monitors

Investigating the motion of the beam, in particular measuring the orbit, is a crucial requirement for achieving efficient accelerator operation. This requires certain devices that allow the determination of the position of the beam along the ring. In general, orbit position is measured using electrostatic pick-ups, which operate based on the effect of induced image charges that collect on an isolated metal plate as shown in Figure 9 due to the field created by the passing beam particles [26]. Such a technique allows a non-destructive measurement

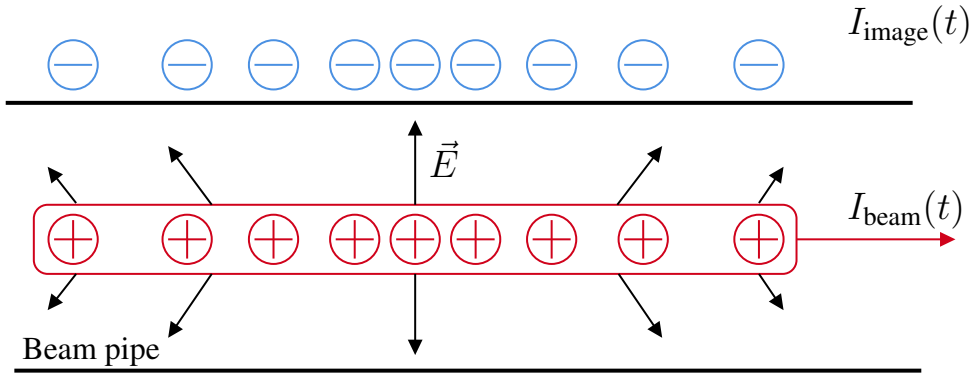


Figure 9: Induced image current $I_{image}(t)$ on the beam pipe wall caused by the positively charged particle flux $I_{beam}(t)$. Adapted from [26].

of the position of the beam. The setup consisting of four pick-ups, with each two of them placed in the horizontal and the vertical plane around the beam pipe, is called a beam position monitor [19].

There are various geometry-specific beam position monitors used on COSY, but diagonal cut BPMs make up the majority of them [27]. For efficient operation and orbit evaluations, such BPMs come in different shapes, cylindrical (Figure 10), used on straight sections, where the beam pipe is round, and rectangular BPMs for arc sections, where the beam pipe has a rectangular shape. The electrodes of each BPM are connected to the amplifiers and the readout electronics. Thus, the offset in x is given by the normalized image voltage difference [29]:

$$x = a \cdot \frac{U_R - U_L}{U_R + U_L}. \quad (3.36)$$

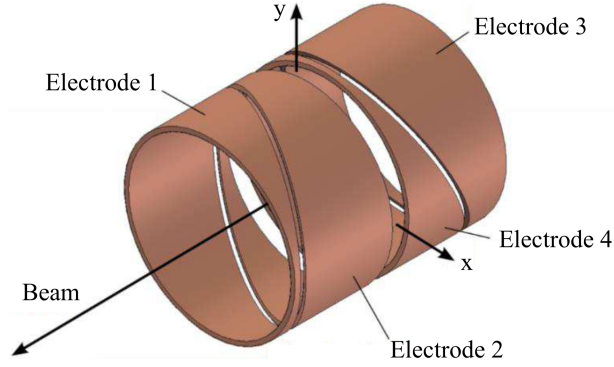


Figure 10: Diagonal cut cylindrical BPM used in COSY. The horizontal and vertical positions of the beam are determined by the voltage differences of electrodes 1 and 2, and electrodes 3 and 4, respectively. Adapted from [28].

The vertical orbit displacement is determined using the same approach, except the signal comes from the “up” and “down” electrodes, giving

$$y = b \cdot \frac{U_U - U_D}{U_U + U_D}. \quad (3.37)$$

The factors a and b in the above formulas represent the calibration factors.

3.5 Longitudinal Particle Motion

Only transverse particle motion within a storage ring has been discussed up to this point. An accelerating cavity, which generates a longitudinal, sinusoidal electric field, affects the particles’ longitudinal motion. In a synchrotron, the radio frequency and the revolution frequency must be synchronized. To achieve this, the circulating particles have to arrive at the cavity at a fixed phase again after each turn [30]. This implies that the frequency of the accelerating field ω_{RF} is an integer multiple of the revolution frequency ω_{rev} [18]:

$$\omega_{RF} = h\omega_{rev}, \quad (3.38)$$

where h is a harmonic number. Therefore, all synchronous particles share the nominal energy and they follow the path of a reference particle. In a bunched beam, if a particle experiences a slight momentum deviation, which affects its horizontal trajectory, it causes a change of

the path length with respect to the reference orbit L_0 [4]. Such a change can be expressed as:

$$\frac{\Delta L}{L_0} = \alpha_p \frac{\Delta p}{p_0}, \quad (3.39)$$

using the momentum compaction factor α_p , which is given by [31]:

$$\alpha_p = \frac{1}{L_0} \int_0^{L_0} \frac{D(s)}{\rho(s)} ds. \quad (3.40)$$

The momentum compaction factor can also decide on a variation of the time of travel of an offset particle relative to the reference particle. Assume, L is a path length, then the revolution time τ of a particle is

$$\tau = \frac{L}{c\beta}, \quad (3.41)$$

where β is the particle's velocity. Then the variation of a revolution time is given by [18]:

$$\frac{\Delta\tau}{\tau} = \left(\alpha_p - \frac{1}{\gamma^2} \right) \frac{\Delta p}{p_0} = \eta \frac{\Delta p}{p_0}, \quad (3.42)$$

where a new factor η is a phase slip factor. Another new quantity from Equation (3.42) is a transition energy γ_{tran} , which can be derived directly from α_p :

$$\alpha_p = \frac{1}{\gamma_{tran}^2} \longleftrightarrow \gamma_{tran} = \frac{1}{\sqrt{\alpha_p}}. \quad (3.43)$$

The transition energy γ_{tran} is the energy for which the momentum compaction vanishes.

For a particle below transition energy ($\eta > 0$), the revolution time is determined by the actual velocity of the particles, which means, that a particle of a higher momentum ($\Delta p/p > 0$), than a reference particle travels faster [31]. For a particle above transition energy ($\eta < 0$), a particle of a higher momentum needs more time for one revolution than a reference particle since the particles are almost at the speed of light, therefore their revolution time depends more on the path length [31].

As mentioned earlier, cavities accelerate the particles by using the electric fields and for a stable operation, it is necessary that the particles in the accelerator arrive at a fixed phase ϕ_s relative to the high-frequency voltage U_0 of a cavity to achieve phase focusing in the longitudinal phase space. The magnetic and cavity fields in a synchrotron both increase synchronously with the particle energy. The energy gain of a synchronous particle per revolution is given by:

$$E_s = qU_0 \sin(\phi_s). \quad (3.44)$$

A particle passing the cavity with a phase deviation $\Delta\phi = \phi - \phi_s$ from a reference phase gains an addition energy ΔE . Such a deviation causes the oscillations of a particle in the longitudinal phase space [20]:

$$\ddot{\phi} + \omega_s^2 \Delta\phi = 0, \quad (3.45)$$

where ω_s is a synchrotron frequency and is defined as:

$$\omega_s = \omega_0 \sqrt{-\frac{eU_0 h \cos \phi_s}{2\pi\beta^2 E} \left(\alpha_0 - \frac{1}{\gamma^2} \right)}. \quad (3.46)$$

Here, stability is reached if ω_s is real and is established by the energy relative to the transition energy γ_{tr} and the phase ϕ itself.

To achieve a desired focusing effect, two cases are to be considered: below transition energy ($\gamma < \gamma_{tr}$): Equation (3.46) is real for $-\frac{n\pi}{2} < \phi_s < \frac{n\pi}{2}$; above transition energy ($\gamma > \gamma_{tr}$): Equation (3.46) is real for $\frac{n\pi}{2} < \phi_s < \frac{3n\pi}{2}$. Therefore, using the above in Equation (3.44) shows that:

1. The phases $-\frac{n\pi}{2} < \phi_s < 0$ decelerate and $0 < \phi_s < \frac{n\pi}{2}$ accelerate the particle. In case, a particle arrives early at a cavity, it gains less energy to travel longer and to appear therefore closer to the synchronous phase next time. On the contrary, the particle gains more energy if it arrives later [31] to reduce its delay next time. Here, the rising flank is used for acceleration.
2. The phases $\frac{n\pi}{2} < \phi_s < \pi$ accelerate and $\pi < \phi_s < \frac{3n\pi}{2}$ decelerate the particle. A particle that arrives earlier at the cavity gains more energy and therefore its revolution time increases, so it arrives later on the next turn and gets closer to the synchronous phase [18]. Analogously, the late particle gains less energy, travels a shorter path, and arrives earlier. In this case, the falling flank of the sinusoidal function is used for acceleration.

Figure 11 depicts the focusing effects for both cases.

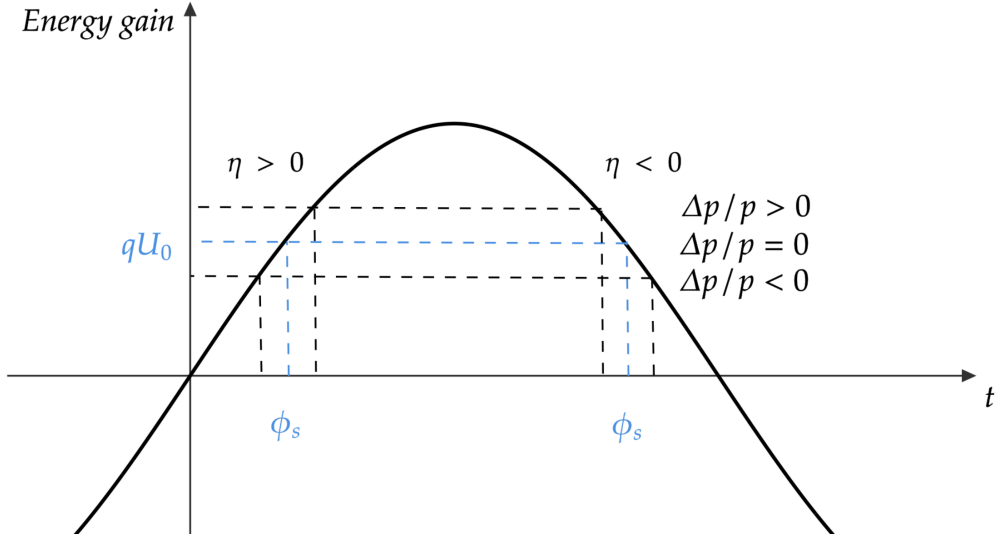


Figure 11: Energy gain as a function of particle phase. For $\gamma < \gamma_{tr}$ the rising flank is used for acceleration, for $\gamma > \gamma_{tr}$ the falling one. Adapted from [19].

3.6 Spin Dynamics

The EDM experiment at COSY is conducted using polarized particles stored in the accelerator. This chapter focuses on spin formalism, polarization, and equations of spin motion inside storage rings.

3.6.1 Spin Formalism

To describe the spin orientation of the particle beam, it is necessary to introduce the polarization P . Generally, a particle can be in any of the spin states with a certain probability distribution. Such a mixed state for a spin- $\frac{1}{2}$ -particle is characterized by a superposition of “up” and “down” states with probabilities $\frac{1}{2}(1 \pm P)$ [32]. In a pure spin state, a particle is considered to be fully polarized along a particular direction. Otherwise, the absence of polarization means, that the particle’s polarization vector $\vec{P} = 0$.

For a particle beam, the polarization P is a statistical average of individual spin vectors of the particles: $P = 0$ if vectors are directed isotropically in all directions and $P = \pm 1$ if particles of the beam share the same pure spin state [33]. Thus, the polarization vector of a

particle ensemble is defined as:

$$\vec{P}_i = \frac{1}{N} \sum_{i=1}^N \vec{S}_i. \quad (3.47)$$

For a beam consisting of spin- $\frac{1}{2}$ -particles ($m = \pm\frac{1}{2}$), polarization vector along the quantization axis is

$$P_V = \frac{N^{m=\frac{1}{2}} - N^{m=-\frac{1}{2}}}{N^{m=\frac{1}{2}} + N^{m=-\frac{1}{2}}}, \quad (3.48)$$

where $N^{m=\frac{1}{2}}$ and $N^{m=-\frac{1}{2}}$ are populations of particles in a particular quantization state.

A similar formalism applies to beams consisting of spin-1-particles. In this case, there are three quantization states $m = \pm 1, 0$. Consider a particle beam containing $N^{m=\pm 1}$ and $N^{m=0}$ particle populations. The vector polarization and tensor polarization along the quantization axis are [34]:

$$P_V = \frac{N^{m=1} - N^{m=-1}}{N^{m=1} + N^{m=0} + N^{m=-1}}, \quad (3.49)$$

$$P_T = \frac{N^{m=1} + N^{m=-1} - 2N^{m=0}}{N^{m=1} + N^{m=0} + N^{m=-1}}.$$

3.6.2 Spin Motion

In the rest frame of a particle, electromagnetic fields interact with the spin via the magnetic and electric dipole moments. This interaction is given by a Hamiltonian in Equation (2.6). In a non-relativistic case spin vector \vec{S} has a form

$$\frac{d\vec{S}}{dt} = \vec{\mu} \times \vec{B} + \vec{d} \times \vec{E} = \vec{\Omega} \times \vec{S}, \quad (3.50)$$

where $\vec{\mu}$ and \vec{d} are given by Equations (2.5). The spin precesses perpendicular to $\vec{\Omega}$ with an angular frequency $|\vec{\Omega}|$. Modifying Equation (3.50) for an accelerator, i.e. curvilinear laboratory reference frame, leads to the Thomas-Bargmann-Michel-Telegdi equation [35], [36]:

$$\frac{d\vec{S}}{dt} = \vec{\Omega} \times \vec{S} = (\vec{\Omega}_{MDM} + \vec{\Omega}_{EDM}) \times \vec{S}, \quad (3.51)$$

where

$$\vec{\Omega}_{MDM} = -\frac{q}{m} \left[G\vec{B} - \frac{\gamma G}{\gamma + 1} \vec{\beta}(\vec{\beta} \cdot \vec{B}) - \left(G - \frac{1}{\gamma^2 - 1} \right) \frac{\vec{\beta} \times \vec{E}}{c} \right], \quad (3.52)$$

$$\vec{\Omega}_{EDM} = -\frac{q}{mc} \frac{\eta}{2} \left[\vec{E} - \frac{\gamma}{\gamma+1} \vec{\beta} (\vec{\beta} \cdot \vec{E}) + c \vec{\beta} \times \vec{B} \right], \quad (3.53)$$

where γ is the relativistic Lorentz factor, η is the parameter describing the strength of the EDM, β is the velocity and G is a gyromagnetic anomaly $G = \frac{g-2}{2}$ with the Lande factor g . Some G -values are presented in Table 2. Expressing the precession due to the MDM in terms of parallel B_{\parallel} and perpendicular B_{\perp} magnetic field components brings it to the form [32]:

$$\vec{\Omega}_{MDM} = -\frac{q}{\gamma m} \left[(1 + \gamma G) \vec{B}_{\perp} + (1 + G) \vec{B}_{\parallel} - \left(G\gamma + \frac{\gamma}{\gamma+1} \right) \vec{\beta} \times \frac{\vec{E}}{c} \right]. \quad (3.54)$$

Due to the coupling of the particle and spin motion, momentum of a particle is to be considered. It precesses with an angular frequency $\vec{\Omega}_{cycl}$ [37]:

$$\frac{d\vec{p}}{dt} = \vec{\Omega}_{cycl} \times \vec{p}, \quad (3.55)$$

with

$$\vec{\Omega}_{cycl} = -\frac{q}{\gamma m} \left(\vec{B}_{\perp} - \frac{\vec{\beta} \times \vec{E}}{\beta^2 c} \right). \quad (3.56)$$

By subtracting Equation (3.56) from (3.54), the following equation is obtained:

$$\Delta \vec{\Omega}_{cycl} = \vec{\Omega}_{MDM} - \vec{\Omega}_{cycl} = -\frac{q}{\gamma m} \left[G\gamma \vec{B}_{\perp} + (1 + G) \vec{B}_{\parallel} - \left(G\gamma - \frac{\gamma}{\gamma^2-1} \right) \vec{\beta} \times \frac{\vec{E}}{c} \right], \quad (3.57)$$

which describes the angular velocity of the spin rotation with respect to the beam direction.

Particle	G
Proton	1.793
Deuteron	-0.142

Table 2: Measured values of the gyromagnetic anomaly G of the particles. Taken from [38].

3.7 Electric Dipole Moment Searches in Storage Rings

The basic principle of an EDM search in the storage rings involves the investigation of the polarized particles. The vertically polarized particle beam is injected into the storage ring,

and the radial electric \vec{E}_x and vertical magnetic fields \vec{B}_y applied are used to trap the particles and store them in the ring. In an ideal storage ring, the MDM contributes to the spin precession only in the horizontal plane. Under the influence of a radial electric field, since $\vec{\Omega}_{EDM} \perp \vec{\Omega}_{MDM}$, a non-zero EDM tilts the spin in a vertical direction (Figure 12), resulting in a vertical polarization oscillation with frequency $\vec{\Omega}_{EDM}$ [39], which is then measured with a polarimeter.

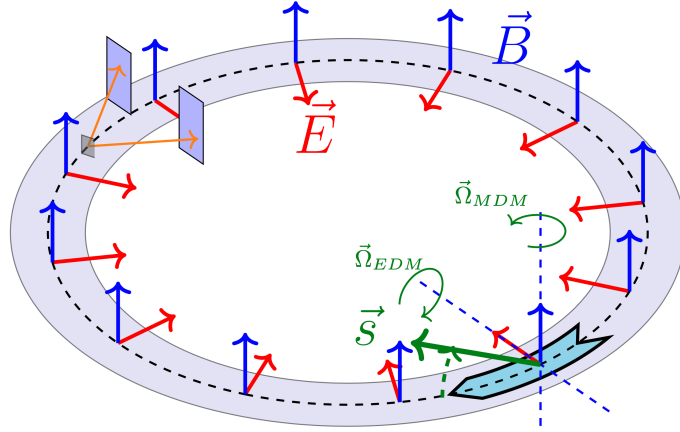


Figure 12: Principle of a storage ring EDM measurement. An EDM tilts the spin \vec{s} in the vertical direction ($\vec{\Omega}_{EDM}$), while MDM causes the spin precession $\vec{\Omega}_{MDM}$ in the horizontal plane. Reprinted from [5].

And as previously mentioned the particles' spin motion is described by a Thomas-BMT Equation (3.51) and is given by:

$$\frac{d\vec{S}}{dt} = -\frac{q}{m} \left[G\vec{B} + \left(G - \frac{1}{\gamma^2 - 1} \right) \vec{v} \times \frac{\eta}{2} (\vec{E} + \vec{v} \times \vec{B}) \right] \times \vec{S}. \quad (3.58)$$

The vertical polarization oscillation in a magnetic ring occurs with a small amplitude $\frac{\eta\beta}{2G}$ [5] representing the ratio of the EDM and MDM contributions from Equations (3.51) and (3.57). The amplitude of an oscillation for the protons and deuterons is too small, which requires different solutions to increase it. One of them is the principle of suppressing the horizontal rotation called a ‘‘Frozen Spin’’ [40]. This method is only applicable to two types of storage rings, those with combined electric and magnetic fields and pure electric storage rings. Both types of storage rings fulfill the criterion

$$\vec{\Omega}_{MDM} = -\frac{q}{m} \left[G\vec{B} - \left(G - \frac{1}{\gamma^2 - 1} \right) \beta \vec{E} \right] \stackrel{!}{=} 0, \quad (3.59)$$

which the Frozen Spin condition can be derived from:

$$G\vec{B} = \left(G - \frac{1}{\gamma^2 - 1}\vec{\beta} \times \frac{\vec{E}}{c}\right). \quad (3.60)$$

COSY, as a classic pure magnetic ring, doesn't employ this method, since it requires a magnetic field \vec{B} to keep the particles in the storage ring, therefore

$$G\vec{B} \stackrel{!}{=} 0 \quad \downarrow \quad (3.61)$$

In this case, an additional element is integrated into the ring to measure the polarization buildup, a Radio Frequency Wien filter [41]. It provides an electric $\vec{E} = (E, 0, 0)^T$ and a magnetic field $\vec{B} = (0, B, 0)^T$. A reference particle passing through a purely magnetic ring with a Wien filter doesn't experience any force due to the vanished Lorentz force, which leaves the particle's trajectory unaffected. Unlike the trajectory and thus the particle's momentum, the spin vector rotates due to the MDM in the horizontal plane, so that it is parallel to the momentum vector of a particle in more or less than 50% of cases [39], which allows the vertical polarization to build up in the dipole magnets of the ring due to an EDM.

4 Cooler Synchrotron COSY

The COSY accelerator facility comprises three main parts: an ion source for polarized and unpolarized H^- and D^- ions, an injector cyclotron JULIC (Juelich Light Ion Cyclotron), and the synchrotron and storage ring COSY. A schematic of COSY is shown in Figure 13. In the injector cyclotron, the H^- or D^- ion beam provided by the source is pre-accelerated to kinetic energies up to 45 MeV and 76 MeV, respectively. The particles are then transferred to the synchrotron through a 100 m long injection beam line (IBL) [42]. Using the stripping

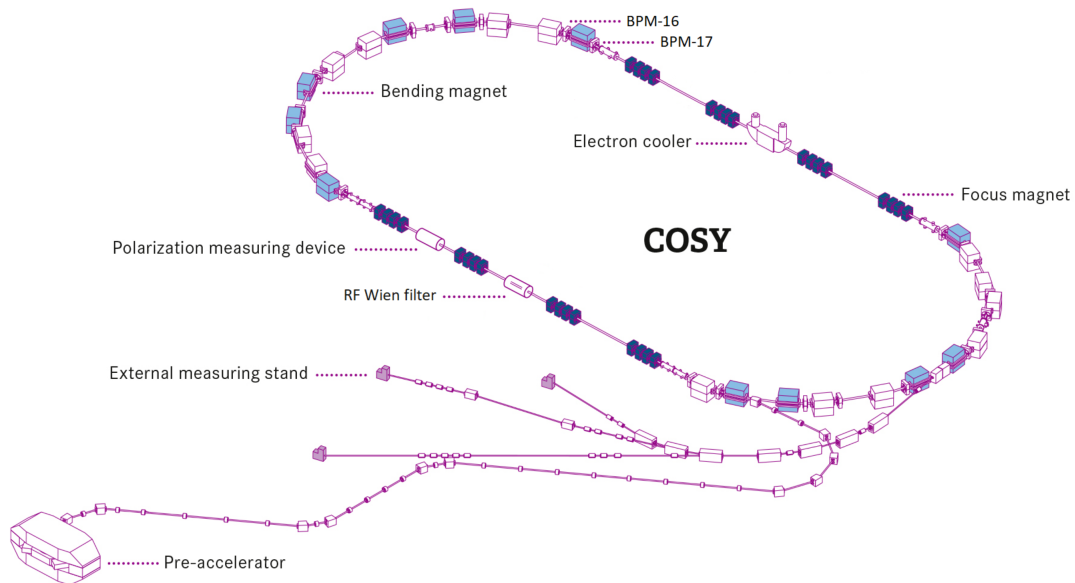


Figure 13: Sketch of the COSY storage ring, the pre-accelerator JULIC, and the injection beamline. Reprinted from [43].

injection the resulting particles, protons or deuterons, enter COSY, where they are accelerated in a radiofrequency (RF) cavity and can reach momenta of $3.7 \text{ GeV}c^{-1}$ [44].

The accelerator ring has a circumference of around 184 m, consisting of two straight sections of 40 m each and two 180° arc sections of 52 m each [45]. The straight sections contain 32 quadrupoles divided into 8 families (MQT1–MQT8), which allows the straight sections to be tuned so that they are used as telescopes with a 1:1 imaging with π or 2π betatron phase advance [45].

The arc sections involve 24 normal-conducting dipoles, which allow the bending of the beam, and 6 quadrupole families (MQU1–MQU6). Each arc consists of three identical elements. The focusing structure in the arc consists of

$$\underbrace{QF - bend - QD - bend}_{\text{Cell 1}} + \underbrace{bend - QD - bend - QF}_{\text{Cell 2}}, \quad (4.1)$$

that enables the interchange of the focusing and defocusing elements [42]. Here, QF stands for a focusing quadrupole, QD for a defocusing quadrupole, and bend for a dipole.

Apart from dipoles and quadrupoles, a total of 17 sextuples, including seven in straight segments and ten in the arcs (families MXS, MXL, MXG), are available for chromaticity changing.

The name of the COoler SYnchrotron originates from the employed cooling systems that are designated to improve phase space density in COSY [46]:

1. electron cooling,
2. stochastic cooling.

The principle of electron cooling resides in shrinking the phase space volume of the beam without removing the particles from the beam [47]. To achieve it, the circulating beam is combined with an electron beam that is injected into the ring. With these electrons being elastically scattered by the particles in the beam, the transverse momentum of the particle beam is reduced [42]. This leads to a reduction of the phase space and a reduction of the beam profile. An additional method – stochastic cooling – is used at COSY for charged particles. Here, the beam is divided into small fractions, so-called “samples”, induced by the pick-ups, and deviations from the optimal orbit are observed.

4.1 Simulation Model

Simulation models for accelerator experiments are an essential part of the research. Models representing a real experimental setup help to investigate particle motions in real accelerators. The following sections discuss the integration of the COSY model into the Bmad program.

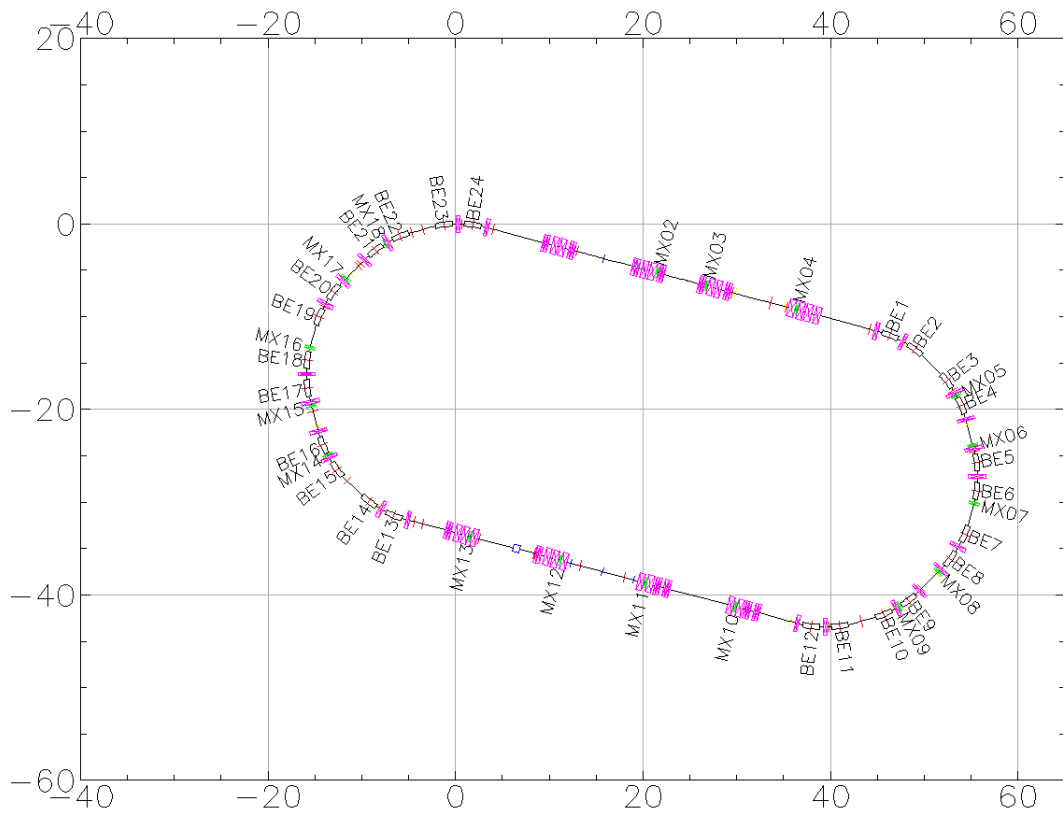


Figure 14: COSY lattice designed in TAO [49]. Lattice includes all of the elements present in the storage ring COSY. For better readability, only the bending magnets (BE1 – BE24) and the sextupoles (green) are labeled in the graph. The quadrupoles are marked in pink.

4.1.1 Implementation into the Bmad Code

Modeling within this thesis is carried out using a software library for relativistic charged single- and multi-particle beam dynamics simulations Bmad [6]. The library has been developed at Cornell University’s Laboratory for Elementary Particle Physics. The library is designed in Fortran90 and is object-oriented [48]. Bmad is familiar with such components as quadrupoles, RF cavities, dipole bends, etc., which made it possible to build a COSY lattice using the Tool for Accelerator Optics (TAO) [49] depicted in Figure 14.

As shown in Figure 14, COSY includes various magnets, such as dipoles, quadrupoles, and sextupoles. As mentioned earlier, the model also includes steerer magnets used for orbit cor-

rection. Furthermore, implemented beam position monitors find their use in orbit matching. In addition to magnets and other elements of the COSY lattice as such, Bmad also allows the incorporation of the effects that influence the model. Such effects include magnet misalignments and effective dipole length, which are still to be touched upon in the course of this thesis (see Sections 4.2 and 4.3).

For a default model, all misalignments, as well as sextupoles and corrector magnets, are turned off. Quadrupoles are also set to their default settings listed in Table 3. For further analysis, including the purposes of this thesis, all the magnet settings of the model can be changed to the actual values of COSY magnets. The data is retrieved from the Experimental Physics and Industrial Control System (EPICS) [50] after each beam time. In this thesis, the data from the latest beam time is used.

Magnet Type	l_{eff} in m
Dipole	1.832596
Quadrupole in arcs	0.372
Quadrupole in straight	0.620
Sextupole G	0.328
Sextupole L	0.243
Sextupole S	0.140

Table 3: Effective lengths of magnets at COSY. Quadrupoles in arcs and quadrupoles in straight sections have different lengths, as well as all three sextupole types. Taken from [51].

Figure 15 shows the optical functions of the default simulation model, beta functions β_x and β_y in horizontal and vertical directions respectively, and horizontal dispersion D_x . The optical settings of COSY are adjusted in a way that the dispersive effects mainly occur in the arc sections. The betatron tunes of a default lattice are $Q_x = 3.632$ in a horizontal and $Q_y = 3.685$ in a vertical direction.

4.1.2 Benchmarking of Particle Motion

Before running the simulation, it is necessary to benchmark it first. Such a test allows for quantifying the numerical limit of the model, which gives information on whether the

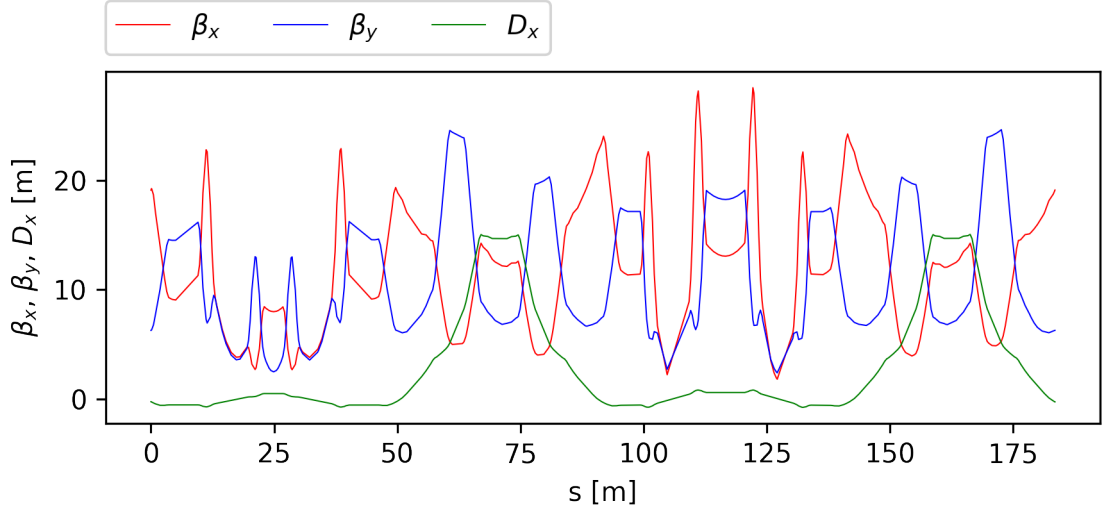


Figure 15: Optical functions β_x , β_y , D_x of the default lattice. The quadrupole settings are adjusted such that dispersion D_x is zero in the straight sections.

model works correctly when additional effects are introduced. The following simulations are performed for protons with a momentum of 530 MeV/c. Benchmarking of the model requires the determination of particle phase space coordinates in six-dimensional phase space in Bmad, which include x , y , z , p_x , p_y and p_z . The transverse coordinates, x and y , of a particle, describe the offset of an orbit from the reference orbit (Figure 16).

The corresponding phase space momenta, p_x and p_y , are momenta \hat{p}_x , \hat{p}_y of a particle in x- and y-directions normalized by a reference particle's momentum p_0 [6], [48]:

$$\begin{aligned} p_x &= \frac{\hat{p}_x}{p_0}, \\ p_y &= \frac{\hat{p}_y}{p_0}. \end{aligned} \quad (4.2)$$

The longitudinal phase space coordinate z is given by [48]:

$$z(s) = -\beta(s)c(t(s) - t_0(s)), \quad (4.3)$$

where $t(s) - t_0(s)$ is the difference in time between the arrival of a circulating particle and the arrival of a reference particle at point s . In turn, the longitudinal phase space momentum p_z is given by a difference between the particle's p and the reference particle's momentum p_0 normalized by the latter [48]:

$$p_z = \frac{p - p_0}{p_0}. \quad (4.4)$$

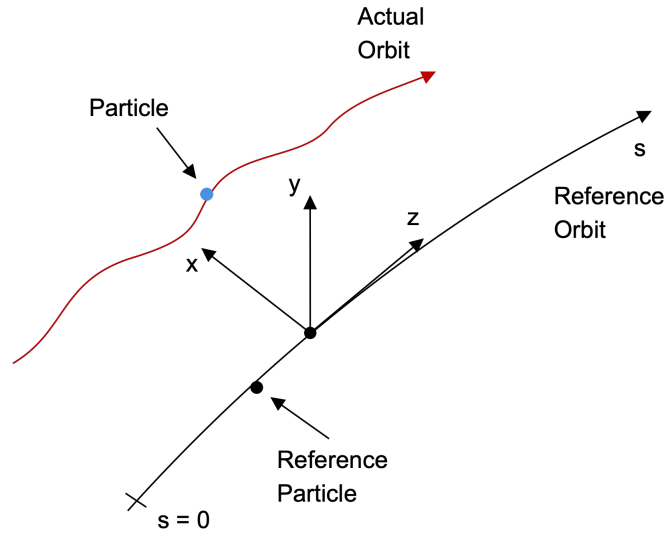


Figure 16: Transverse coordinates x and y describe the offset of an actual orbit from a reference orbit. Adapted from [48].

Based on this information, an investigation of the closed orbit of the COSY model can now be performed. The closed orbit is calculated using the Bmad `closed_orbit_calc` subroutine [48]. As can be seen in Figure 17, some phase space coordinates of the closed orbit vary around the circumference of the ring. The horizontal and longitudinal phase space coordinate plots reveal some numerical noise, while the vertical phase space remains to lie precisely at zero. Such a difference is due to an absence of influence of dipoles on the vertical phase space. Despite some distortions in the upper four plots, the values of the closed orbit in each section of the circle along the circumference s are still insignificant, as they have magnitudes from 10^{-12} to 10^{-15} . To check that such a minor numerical noise indeed does not affect a particle moving in a closed orbit, it is necessary to track it over numerous turns. The multi-turn tracking through the lattice was done using a subroutine `track_all`. The results of tracking for over 10.000 turns proved that the numerical noise does not affect the observed particle, by the fact that there are no deviations in the horizontal, vertical, and longitudinal phase space. Hence, the observed particle can be considered as a reference particle for further analysis.

At this point, the model's performance can be investigated. To begin with, it is worth checking how the three-dimensional phase space behaves for the particles with different initial

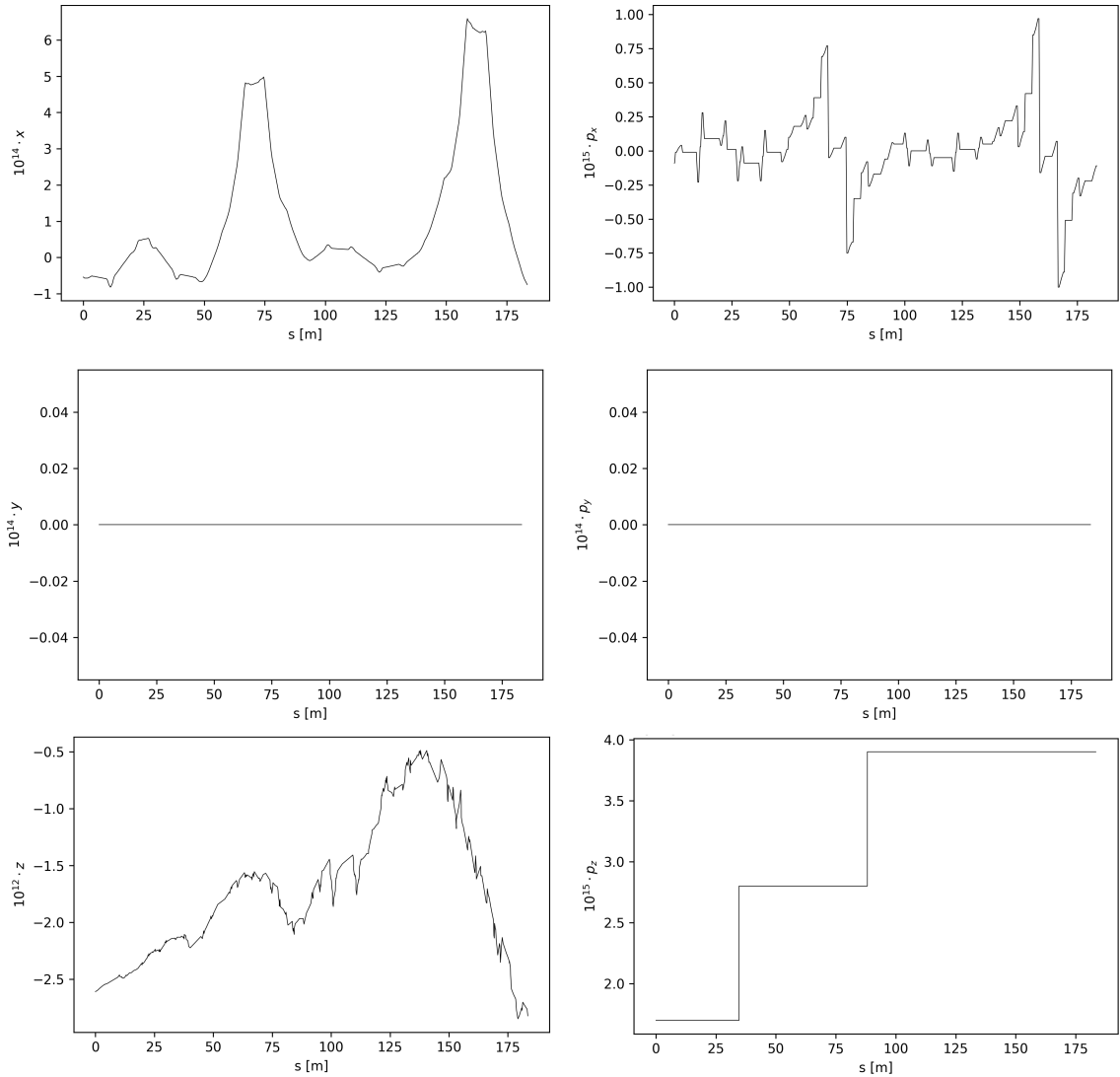


Figure 17: Closed orbit of a COSY lattice calculated using the `closed_orbit_calc` subroutine. The plots reveal the deviations of the horizontal, vertical, and longitudinal phase space coordinates (from top to bottom). The x-axis gives a position s on the ring.

phase space coordinates. Figure 18 demonstrates the three-dimensional phase space of a particle with an initial horizontal offset. For this study, a horizontal shift $\Delta x = +0.001$ m was chosen, and the simulation was done for 10,000 turns. In the first graph on the left, a phase space ellipse is shown in the horizontal direction. However, in the vertical direction, the particle does not experience any effect of this offset. As was mentioned earlier, in an ideal circular accelerator the vertical and horizontal motions of the particles are decoupled

[52], [18], which is also a case for the COSY model. The resulting ellipses in the longitudinal direction indicate that the particle, due to its horizontal shift, moves no longer along the reference orbit, but along a lengthy path, which causes the difference between the arrival phase and the reference phase, leading to a shift of the center of an ellipse to a new equilibrium momentum.

The same offset was chosen for the vertical motion. As can be seen in Figure 18, the phase space ellipse is now represented in the vertical and longitudinal phase space. The distortions in the horizontal phase space are caused by the fact that the offset particle experiences the non-vanishing dispersion in the arcs of COSY [51].

As shown in Figure 29 in Appendix A, the vertical phase space of the particle remains unchanged, when shifted in the longitudinal direction. However, as expected, the horizontal phase space is affected by the offset, since the particle is moving along the dispersive trajectories of the COSY and its motion is determined by the betatron oscillations [51].

4.2 Magnet Misalignments

The simulation has so far assumed an ideal model, i.e. all the magnets are positioned ideally and the influence of closely spaced elements is neglected. For understanding the transverse beam deviations within COSY, it is very important to consider and quantify the impact of possible effects on the particles. One of the sources influencing the beam propagation in the ring is the strength and location of the magnets.

Both quadrupoles and dipoles can be shifted along all three axes, as well as can rotate around them. If the quadrupoles are misaligned, the particle beam follows a different path through the magnet, and therefore, the closed orbit is shifted as well [53]. Such shifts appear to have the most influence since shifts in the x and y directions result in changes in the force acting on the particle passing through, even for those moving along the magnetic axes.

Misplacements and rotations of the bending magnets certainly affect the orbit as well. For a longitudinally shifted dipole, for example, the bending of the beam passing through it will be changed in the horizontal direction [54]. And in the case of rotation of the dipole around its longitudinal axis, the vertical magnetic field decreases, and a horizontal component is to be considered [55].

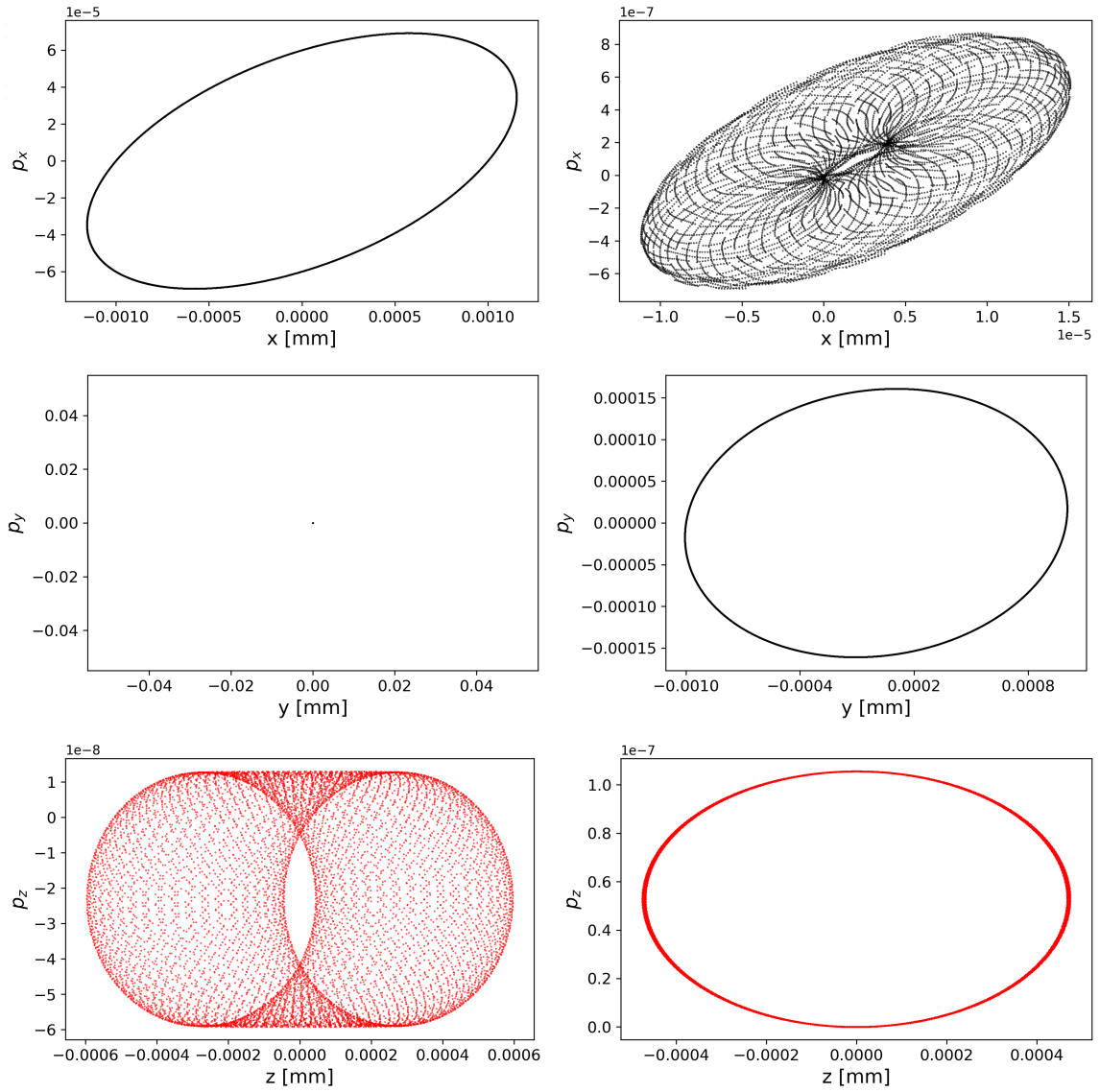


Figure 18: Left column: three-dimensional phase space of a particle with a horizontal offset Δx . Due to the dispersive effects, various ellipses appear in the longitudinal phase space. Right column: three-dimensional phase space of a particle with a vertical offset Δy . The distortions in the horizontal phase space result from the non-vanishing dispersion in the arcs.

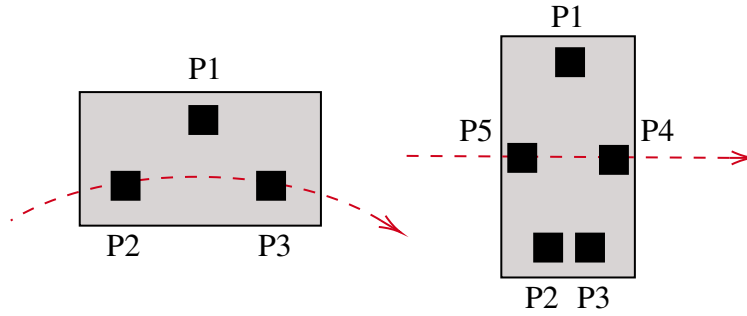


Figure 19: Reference marks P1 – P5 on top of the COSY dipoles (left) and quadrupoles (right). The red dashed line is the beam path. Adapted from [57].

Previous investigations [51] have already established that magnet displacements contribute significantly to the deviations of the closed orbit. To reduce the effect of magnet misalignments, they must be identified and eliminated as effectively as possible. To determine the current position of each particular magnet at COSY, the laser-based measurements are performed by the external company Stollenwerk [56]. The magnets have reference marks on top, dipoles have three, and quadrupoles have five (see Figure 19). In Figure 19 on the left, on a dipole, the two nearest points to the reference orbit are P2 and P3. For the quadrupoles, the points lying right above the symmetry point are P4 and P5. The position measurement performed by Stollenwerk [56] is carried out according to these reference points. The last survey was conducted in 2019 and the results as well as the measurement uncertainties are presented in Figure 20 and Appendix B.

4.3 Dipole Shortening

Another systematic effect influencing the orbit is the effective length of the magnet. In this work, such a phenomenon is only considered for the dipoles. In general, the effective length of a magnet mounted into the accelerator can be influenced by the field of the surrounding magnets due to their close positioning. L.H.A. Leunissen [58] investigated this question for the COSY accelerator, managing to roughly estimate the values of the effective dipole lengths.

The simulations by L.H.A. Leunissen [58] show, that the effective length of the COSY dipole is affected by a close-by steerer magnet, which interacts with the fringe fields of the dipole

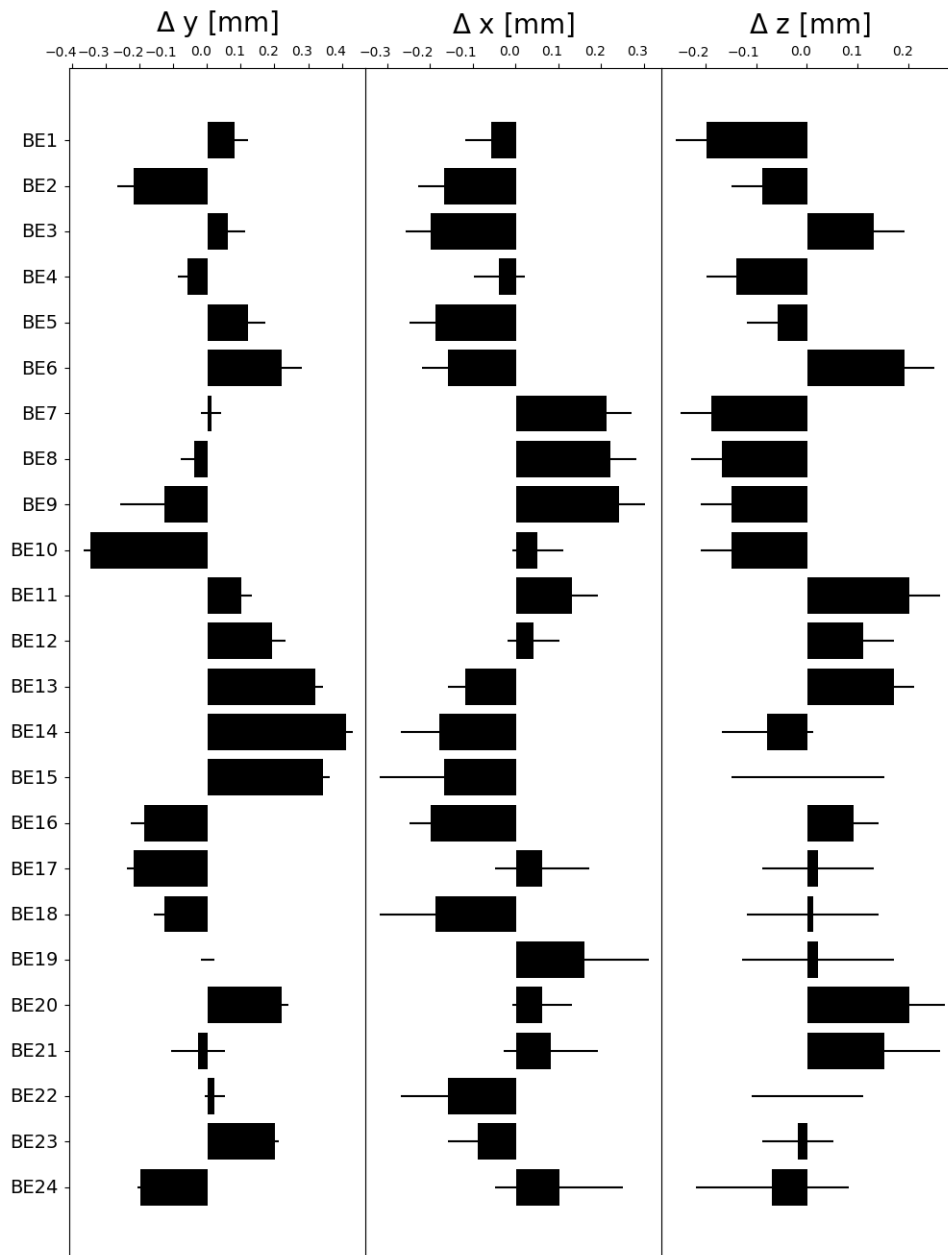


Figure 20: Mechanical misalignment of the COSY dipoles including the measurement uncertainties. Δz gives a displacement in a longitudinal, Δx and Δy in horizontal and vertical directions, respectively. The measurements were conducted in 2019 by Vermessungsbüro Stollenwerk [56].

and thus shortens its effective length. This change directly affects the bending such that it no longer corresponds to the original bending of 15 degrees. Thus, in a simulation [58] an H-type steerer was placed at a distance of 216 mm from the dipole. According to the study, this reduced the effective length of the dipole by 0.34%. The same measurements with a C-steerer positioned 222 mm from the dipole showed that the length was 0.26% shorter. The effect that orbit experiences from dipole shortening is received as a kick inside a dipole. Rough estimations for such kicks have already been made by H. J. Stein [59]. They are mainly based on field calculations by considering the distances between the magnets. Furthermore, the latest values of the dipole lengths have been determined by M. Hartmann [60] in early 2022 straight from the measured orbits by fitting. Figure 21 shows that the dipole shortening

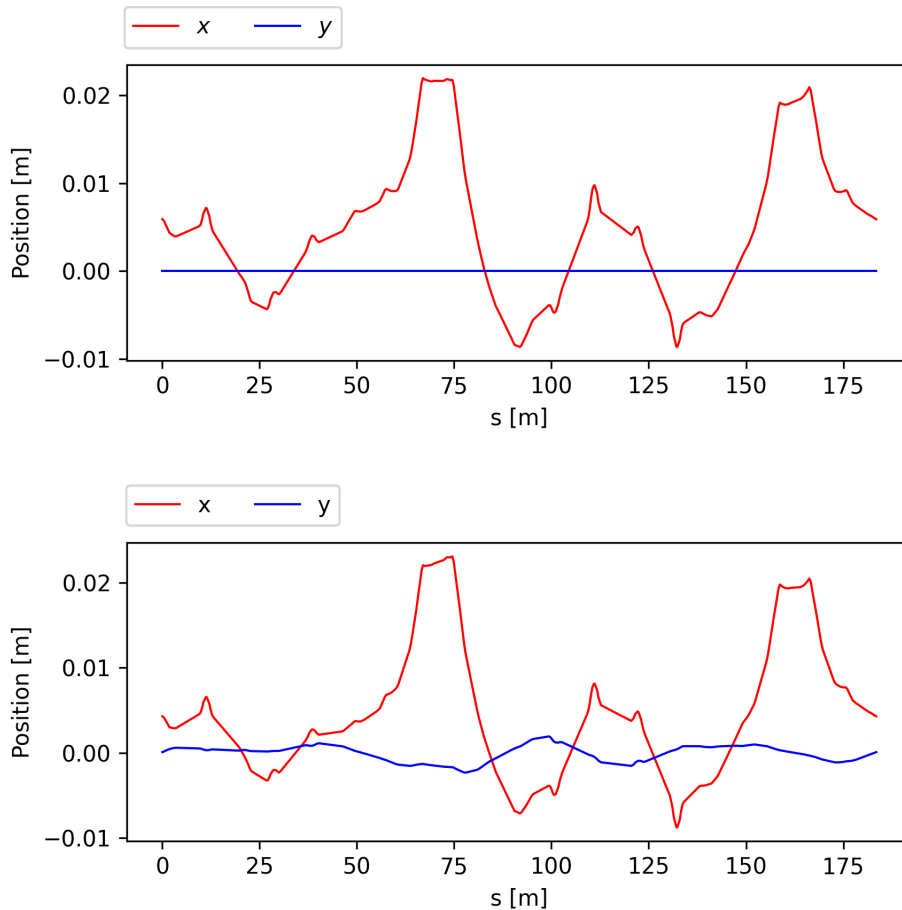


Figure 21: Horizontal x and vertical y closed orbits resulting from dipole shortening effect with an underlying ideal lattice (top) and including magnet misalignments (bottom).

significantly influences the horizontal orbit, while the vertical orbit is not affected at all.

During one of the beam times, in 2019, the orbit correction was turned off. This allowed the impact of the changed effective dipole length in the orbit to be observed. According to the simulation done by V. Poncza in [51], the model including the effect of the dipole shortening showed great agreement with the measured orbits. Incorporation of such a phenomenon into the simulation helps to better describe the real setup and therefore this effect is included in all simulations.

5 Model Fitting and Data Analysis

In the previous section, the various systematic effects that have been added to the simulation were discussed, and their effect on the closed orbit in COSY was described. Such analysis was done to better understand and control the impact of these effects on the orbit in the future. Thus, to see how well the model reflects reality, taking into account such factors as magnet displacements and studies of the effective dipole lengths, it is necessary to compare the results measured at COSY with the simulation model. Moreover, in this section, some complex algorithms for model fitting are introduced, which help to describe a real machine better.

The strength values for the main magnets, dipoles, quadrupoles, and sextupoles, as well as for the steerer magnets are taken from the beam time of February – March 2022. Figure 22 shows the simulated and the measured closed orbits in comparison. The simulated and measured betatron tunes are summarized in Table 4.

	Simulated	Measured
Q_x	3.632	3.545
Q_y	3.685	3.619

Table 4: Simulated and measured betatron tunes Q_x and Q_y for the same magnet settings.

The tunes do not match their measured values, and it is clear from Figure 22 that the simulated orbits do not match the real orbits. While the vertical orbit at least roughly resembles the real COSY orbit, the horizontal orbit does not correspond to the measurement at all.

During the beam time, the orbit correction was turned on at all times in order not to lose the beam immediately. Thus, it should be noted that the steerers have a substantial impact on the orbit and the new values need to be calculated for a better match. As of today the recalculation of the kicker values is not possible due to the calibration factors [51] which must also be determined for the actual setup. In further analysis, the corrector strengths are estimated to bring the simulated orbit closed to the measured one.

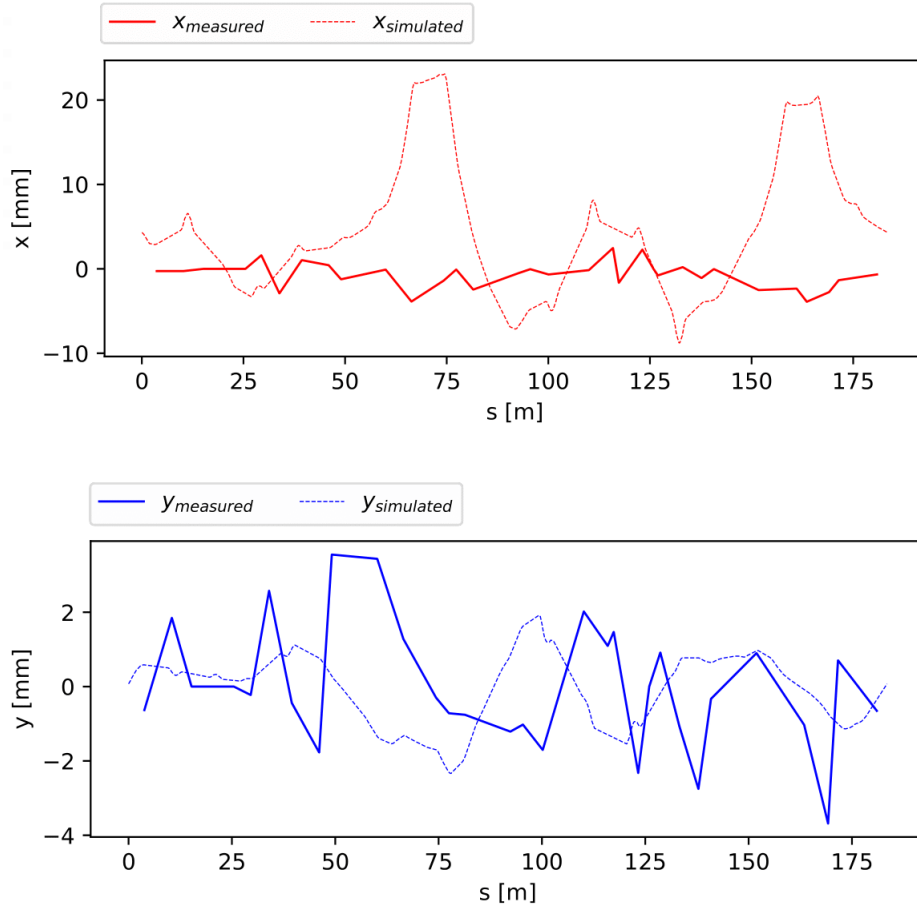


Figure 22: Simulated and measured horizontal x and vertical y orbits. The simulation includes the same magnet settings used during the run in February – March 2022, as well as the changed effective dipole lengths and the magnet misalignments.

5.1 Orbit Correction

Since the magnetic structure of the accelerator makes it impossible to build it perfectly and there are always such systematic effects as effective magnetic length as well as magnet alignments, and the closed orbit, therefore, deviates from the ideal trajectory, it is necessary to implement an orbit correction system. To provide an orbit resembling the desired target orbit, additional smaller dipoles are used to guide the beam in the vertical and horizontal directions. For these correcting magnets to most accurately bend the beam around the accelerator, the exact configuration of the field strength of these dipoles must be calculated from the extent

to which each of them affects the orbit. The orbit's response to these dipoles' influence is measured using beam position monitors (BPM).

5.1.1 Orbit Response Matrix Calculation

The connection between the changes in dipole magnet strengths and the motion of the beam particle at the beam position monitor is established by the orbit response matrix (ORM).

Assuming m BPMs and n corrector magnets, the beam offsets are denoted by $\Delta\vec{x}$ and steerer kicks by $\Delta\vec{k}$, the orbit response to the perturbations at the steerer magnets is given by [61]:

$$\Delta\vec{x} = \mathbf{R}\Delta\vec{k}, \quad (5.1)$$

where \mathbf{R} is a $m \times n$ -dimensional orbit response matrix.

The corresponding matrix element R_{ij} containing the response of a BPM i ($i = 1, \dots, m$) to the changes in a corrector j ($j = 1, \dots, n$) is calculated as [62]:

$$R_{ij} = \frac{\sqrt{\beta_i\beta_j}}{2 \sin(\pi Q)} \cos(\phi_i - \phi_j - \pi Q), \quad (5.2)$$

where Q is the betatron tune of the machine, $\beta_{i,j}$ and $\phi_{i,j}$ denote beta and phase functions of the i -th BPM and j -th corrector magnet.

Bmad makes the calculation of the matrix for COSY with settings for the main quadrupoles as well as for the correcting magnets possible, using data obtained in February – March 2022.

The calculated ORM is displayed in Figure 23.

The result of a successful orbit correction is the determination of the correct magnet strengths which stipulate the approximation to the target orbit. The goal of the thesis is to match the model \vec{x} not to an ideal orbit, but to a measured orbit \vec{x}_{tar} at COSY. To approach this problem, it is necessary to first calculate the difference between the values of the target and simulated orbits:

$$\Delta\vec{x} = \vec{x}_{tar} - \vec{x}. \quad (5.3)$$

Based on Equation (5.1), the magnet strengths \vec{k} are calculated using the general formula:

$$\Delta\vec{k} = -\mathbf{R}^{-1}\Delta\vec{x}. \quad (5.4)$$

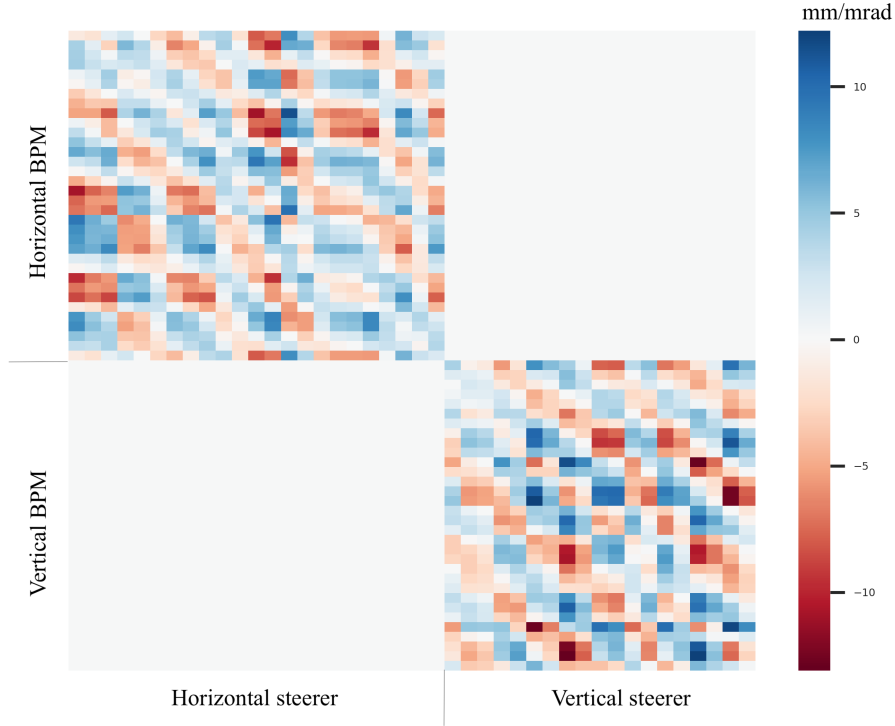


Figure 23: Orbit response matrix of an optical model. It is used to describe the accelerator and usually does not correspond with a measured ORM [61].

In case there are no analytical solutions satisfying this equation, it is necessary to find one that minimizes the difference [62]:

$$|\mathbf{R} \cdot \Delta \vec{k} - \Delta \vec{x}| \rightarrow \min. \quad (5.5)$$

To achieve this, a pseudo-inverse of the matrix \mathbf{R} is to be calculated. The common way to produce a pseudo-inverse is a singular value decomposition (SVD) method [63], which is described in the next section.

5.2 Orbit Matching Procedure

As mentioned before, for the thesis and the project itself, the target orbit is set to be the measured orbit at COSY. The elements of the ORM of the simulation R_{ij}^{sim} are calculated by Equation (5.2). Since the number of BPMs at COSY ($m = 67$) is larger than the number of

steerer magnets ($n = 43$), the inverse of the orbit response matrix is calculated via singular value decomposition.

5.2.1 Singular Value Decomposition

The singular value decomposition of a real matrix $\mathbf{R} \in \mathbb{R}^{m \times n}$ is expressed by

$$\mathbf{R} = \mathbf{U} \cdot \mathbf{S} \cdot \mathbf{V}^T, \quad (5.6)$$

where \mathbf{S} is a diagonal real $m \times n$ -matrix with the non-negative eigenvalues s_i [64]:

$$\mathbf{R} = \mathbf{U} \cdot \begin{pmatrix} s_1 & 0 & \cdots & 0 \\ 0 & s_2 & \cdots & 0 \\ & \cdots & \cdots & \\ 0 & 0 & \cdots & s_n \end{pmatrix} \cdot \mathbf{V}^T, \quad (5.7)$$

with $s_1 > s_2 > \dots > s_i$. The unitarity of the matrices $\mathbf{U} \in \mathbb{R}^{m \times m}$ and $\mathbf{V} \in \mathbb{R}^{n \times n}$ implies:

$$\mathbf{U}\mathbf{U}^T = \mathbf{V}^T\mathbf{V} = \mathbf{1}. \quad (5.8)$$

For the calculations in this thesis, the actual layout of COSY, where $m > n$, was taken into account. Thus, the solution to the minimization problem (5.5) is given by:

$$\begin{aligned} \Delta \vec{k} &= (\mathbf{R}^T \mathbf{R})^{-1} \mathbf{R}^T \Delta \vec{x} \\ &= ((\mathbf{U}\mathbf{S}\mathbf{V}^T)^T (\mathbf{U}\mathbf{S}\mathbf{V}^T))^{-1} (\mathbf{U}\mathbf{S}\mathbf{V}^T)^T \Delta \vec{x} \\ &= (\mathbf{V}\mathbf{S}\mathbf{U}^T \mathbf{U}\mathbf{S}\mathbf{V}^T)^{-1} (\mathbf{V}\mathbf{S}\mathbf{U}^T) \Delta \vec{x} \\ &= (\mathbf{V}\mathbf{S}^{-2}\mathbf{V}^T) (\mathbf{V}\mathbf{S}\mathbf{U}^T) \Delta \vec{x} \\ &= \mathbf{V}\mathbf{S}^{-1}\mathbf{U}^T \Delta \vec{x}. \end{aligned} \quad (5.9)$$

5.3 Analysis of the Simulation Results

The orbit matching algorithm was performed using the LAPACK routine for Fortran [65]. Orbit matching is generally carried out separately for horizontal and vertical orbits. The principle of the algorithm is the same for both of them:

1. Initially, the program selects all the horizontal and vertical BPMs from the COSY lattice and records them, together with the transverse coordinates x and y of the simulated orbit. Then the corrector magnets are listed (horizontal kickers for `x_orbit_match` and vertical kickers for `y_orbit_match` subroutines).
2. The matching algorithm calculates the difference between the values of the target and simulated orbits $\Delta\vec{x}$ according to Equation (5.3).
3. The LAPACK routine [65] mentioned above uses the singular value decomposition method (see 5.2.1) to calculate the pseudo-inverse of an ORM. The products of the elements of the pseudo-inverse with $\Delta\vec{x}$ provide the corrections, i.e. steerer settings. The settings as well as the resulting closed orbit are stored after each iteration.
4. The sum of all corrections after each iteration represents the final steerer magnet settings, which allow the simulated orbit to be adjusted to the measured one.

Before proceeding directly to matching the obtained orbits, it is necessary to ensure that the algorithm is efficient by running a benchmark test. The ultimate goal of the test is to fully distort the default orbit. To make sure the matching algorithm described above works correctly it is necessary to run the test as follows:

1. Set all steerer values to 0. In this way, the default orbit is initially not distorted at all. For the test, the target orbit is the design orbit ($x, y = 0$).
2. Apply a random kick to a certain steerer magnet in the default model. Run the matching algorithm to see how the algorithm handles single kicks.
3. Apply random kicks to all steerer magnets in the default model. Run the matching algorithm several times and calculate the final steerer settings.

Table 5 shows the results of the benchmarking of the vertical orbit matching procedure after two iterations. For clarity, the values of some undistorted steers are included in the table. Here, the kick value of the MSV02 steerer was set to -0.1 mrad. As can be seen, the correction for MSV02 is 10^{-4} after the first iteration, thus eliminating the initial distortion. After the second iteration, the value for MSV02 already reaches zero.

Steerer	Correction after 1 st iteration	Correction after 2 nd iteration
MSV02	$1.00 \cdot 10^{-4}$	$-1.08 \cdot 10^{-11}$
MSVBLW1	$-5.95 \cdot 10^{-11}$	$5.95 \cdot 10^{-11}$
MSVBLW4	$2.30 \cdot 10^{-10}$	$-2.30 \cdot 10^{-10}$
MSV06	$-3.11 \cdot 10^{-10}$	$3.11 \cdot 10^{-10}$
MSV08	$9.85 \cdot 10^{-11}$	$-9.85 \cdot 10^{-11}$

Table 5: Results of the benchmarking of the `y_orbit_match` subroutine for the first five steerers with an initial MSV02 kick value $k = -0.1$ mrad. Values of the other steerer magnets are set to 0.

The final setting of MSV02 is the sum of the corrections after two iterations. The same test has been performed for the horizontal orbit, demonstrating similar results.

The next step is benchmarking the algorithm for the fully distorted orbit. The random kick values are drawn from a normal distribution and thus are given by:

$$\Delta k_i = \mathcal{N}(0, 0.0005 \text{ rad}), \quad (5.10)$$

where k_i are the corrector magnets with $i \in \{1, \dots, n\}$. The matching algorithm is then applied to a distorted orbit and executed several times. Following each iteration, the settings of the corrector magnets are recorded. The evolution of the kick values can be seen in Figure 24. Monitoring the dynamics of the values is useful to determine how far the algorithm is from solving the problem. Figure 24 shows that after the first iteration the values are still fairly large, and only after the third iteration they drop significantly, approaching values close to zero. This progress is also represented by the root mean square (RMS) trend of the closed orbits. The RMS values give the square root of the arithmetic mean of the squares of the positions of the x and y orbits. Figure 25 illustrates how the closed orbit RMS values decrease and reach the magnitude of about 10^{-11} .

Next, the model is to be matched to the measured orbit. This is done by activating all the orbit-influencing effects and randomizing the kick values as previously done. Similar to the process described above, Figure 26 shows how after a certain number of iterations the RMS

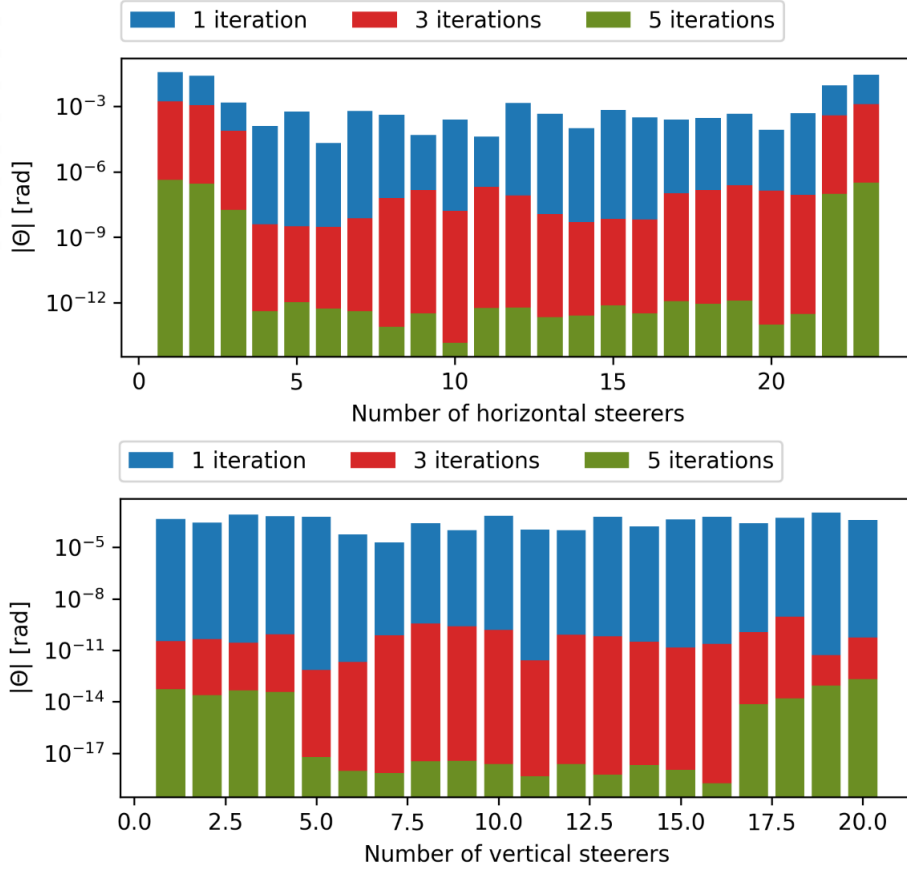


Figure 24: Evolution of the steerer kick values after 1, 3, and 5 iterations of the orbit matching procedure of a default model. The matching result improves after each iteration adjusting the kick values such that the orbit becomes less distorted. After the 5th iteration the values of the steerers reach zero.

values of both closed orbits reach the RMS values of the measured orbits:

$$\begin{aligned}
 RMS_{x,measured} &= 1.6313 \text{ mm}, \\
 RMS_{y,measured} &= 1.6088 \text{ mm}.
 \end{aligned}
 \tag{5.11}$$

The RMS of the vertical and horizontal closed orbits approach the desired values already after the second iteration, and after the 3rd one they drop slightly lower. These values then remain roughly the same, which means that further iterations are insignificant for the matching procedure and can be neglected.

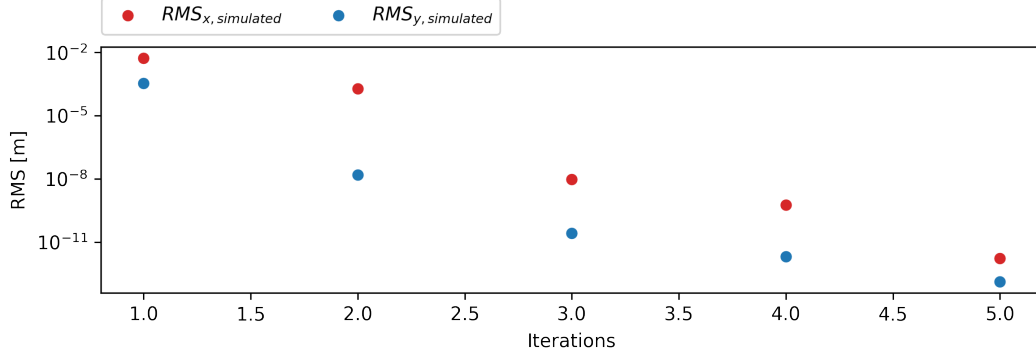


Figure 25: RMS values trend of the simulated orbits after each iteration of the orbit matching algorithm. The default orbit is distorted by the normally distributed steerer kicks. Benchmarking shows that after the 5th iteration the RMS values of the closed orbits are reduced by more than 7 orders of magnitude.

Therefore, the final RMS values after the 3rd iteration are:

$$\begin{aligned} RMS_{x,final} &= 1.6425 \text{ mm}, \\ RMS_{y,final} &= 1.5904 \text{ mm}. \end{aligned} \quad (5.12)$$

The final step in correcting the simulated orbit is to test the calculated magnet kicks. The data stored after each iteration are added up to a final setting of a steerer magnet. The orbits obtained after three iterations, as well as the measured orbits for comparison, are displayed in Figure 27. The corresponding final steerer settings are shown in Figure 28 and Figure 33 in Appendix C. The changed values of the steerer magnets have a strong impact on the orbits, which allows the simulation to describe measured orbits significantly better. However, the adjusted steerer strengths do not eliminate the discrepancies between the orbits. In principle, a perfect match is not to be expected as this cannot be achieved with a different number of BPMs and steerers. As described earlier, the predicted orbit shift is calculated according to Equation 5.1, which can be rewritten in a form of column vectors \vec{u}_i and \vec{v}_i of the matrices \mathbf{U} and \mathbf{V} , respectively:

$$\Delta\vec{x} = \sum_{i=1}^{\min(m,n)} s_i \vec{u}_i (\vec{v}_i^T \Delta\vec{k}), \quad (5.13)$$

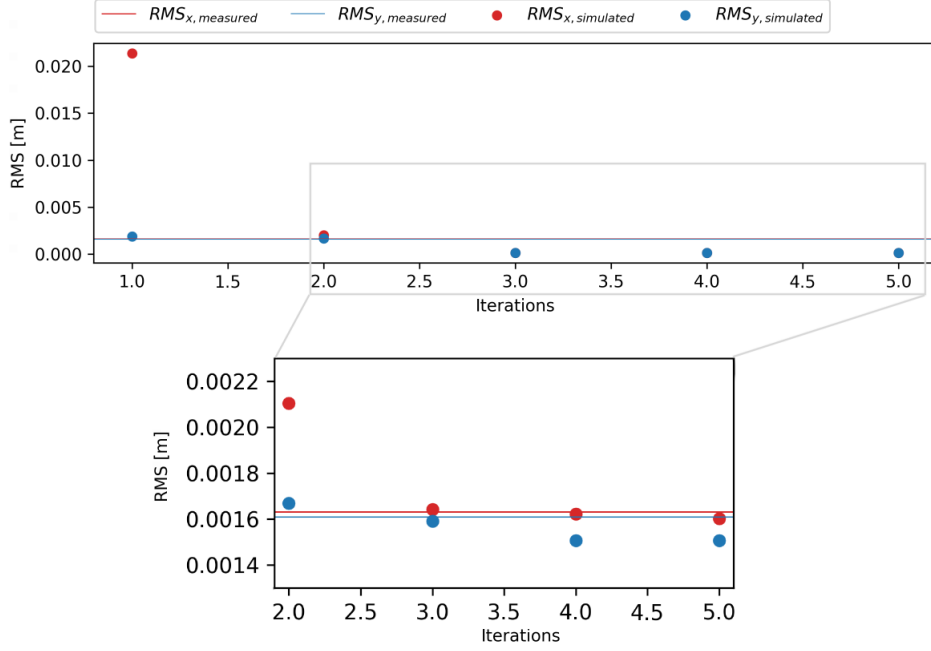


Figure 26: RMS values trend of the horizontal and vertical orbits after each iteration of the orbit matching algorithm. The RMS values of both orbits approach the measured RMS values after the 2nd iteration and remain roughly constant after the 3rd one.

where the eigenvalues s_i determine the magnitude of orbit changes. Based on Equation 5.13, a large eigenvalue s_i is effective and has a strong impact on the orbit change, while small and eigenvalues equal to zero have little or no effect on the orbit at all. To better understand the correlation between the corrector strengths from Figures 28 and 33 and resulting orbit changes displayed in Figure 27, Equation 5.9 can also be represented in a singular value (SV) mode [66]:

$$\Delta \vec{k} = \sum_{i=1}^{\min(m,n)} \frac{1}{s_i} \vec{v}_i (\vec{u}_i^T \Delta \vec{x}). \quad (5.14)$$

The dot-product of the vectors \vec{u}_i with the difference in the position $\Delta \vec{x}$ represent the so-called projection of the target orbit shift in the i-th SV mode [66]. The factor s_i is taken into account to calculate the final steerer settings as well. As can be seen in Equation 5.14, the inverse dependence ($\frac{1}{s_i}$) emerges: if the eigenvalue s_i is very small, the larger steerer strengths are needed for an orbit correction. Thus, for the simulated orbit to approach the target one at positions where $\Delta \vec{x}$ is small, the steerer kick is smaller, which means that the eigenvalue s_i

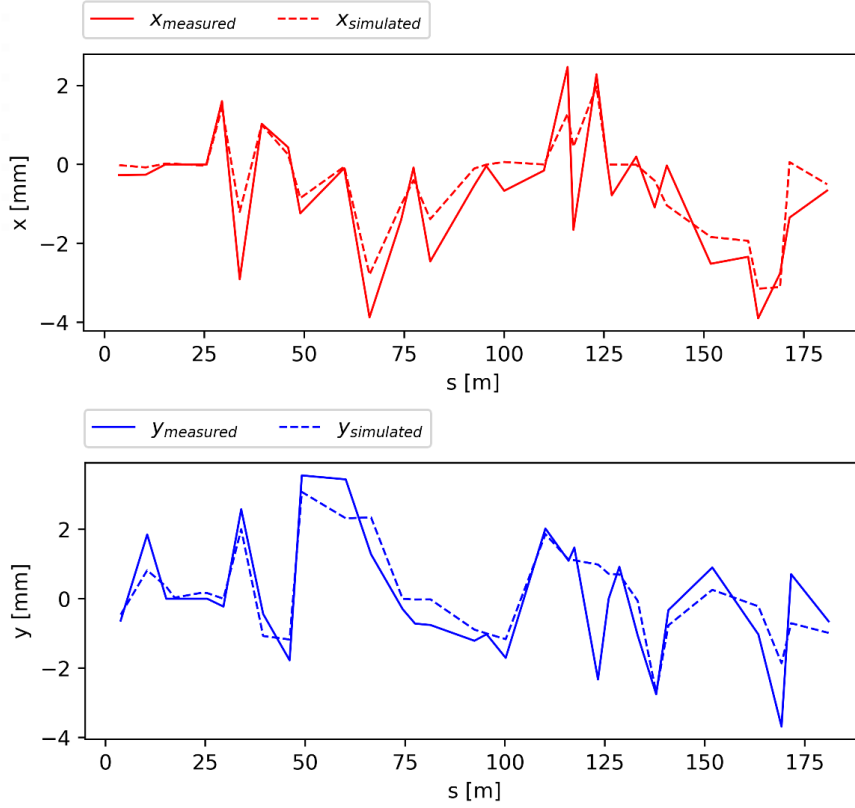


Figure 27: Results of the orbit matching procedure. The simulated horizontal and vertical orbits resemble the measured ones already after the 3rd iteration. The steerer magnet values used to obtain this result are presented in Figures 28 and 33.

for a given position has a larger value. Otherwise, where $\Delta\vec{x}$ is large, a stronger kick value is used. To avoid unrealistic solutions for $\Delta\vec{k}$, when s_i takes an excessively small value, it is necessary to set the maximum allowed kick change. For the simulations done, the threshold was set to 2 mrad.

Despite the fact that the orbit matching algorithm does not help to perfectly describe the measured orbits, the result is relatively accurate. Such a conclusion is inferred from the obtained RMS values. According to the results in (5.11) and (5.12), the RMS values for both orbits are in a good agreement. The explanation may lie in the mostly well-estimated values of the correctors, which allow for getting as close to the measured orbits as possible. Thus, the mean values of the squares at each position of the x and y orbits correspond well to each

other.

Possible sources affecting the accuracy of the algorithm may also include the influence of the quadrupoles and dipoles on the orbit, which cannot be locally compensated by the steerers, as they are located between the main magnets. Besides the systematic effects introduced earlier and implemented into the model, there are various other effects, such as BPM misalignment described by T. Wagner in [27] and effective quadrupole strength studied by L.H.A. Leunissen [58]. Such effects have not been investigated in the framework of this thesis, thus their impact should not be underestimated beforehand. It is likely that a model capable of describing the COSY orbit already at this stage can approach it even more closely if other effects are taken into account in the simulation.

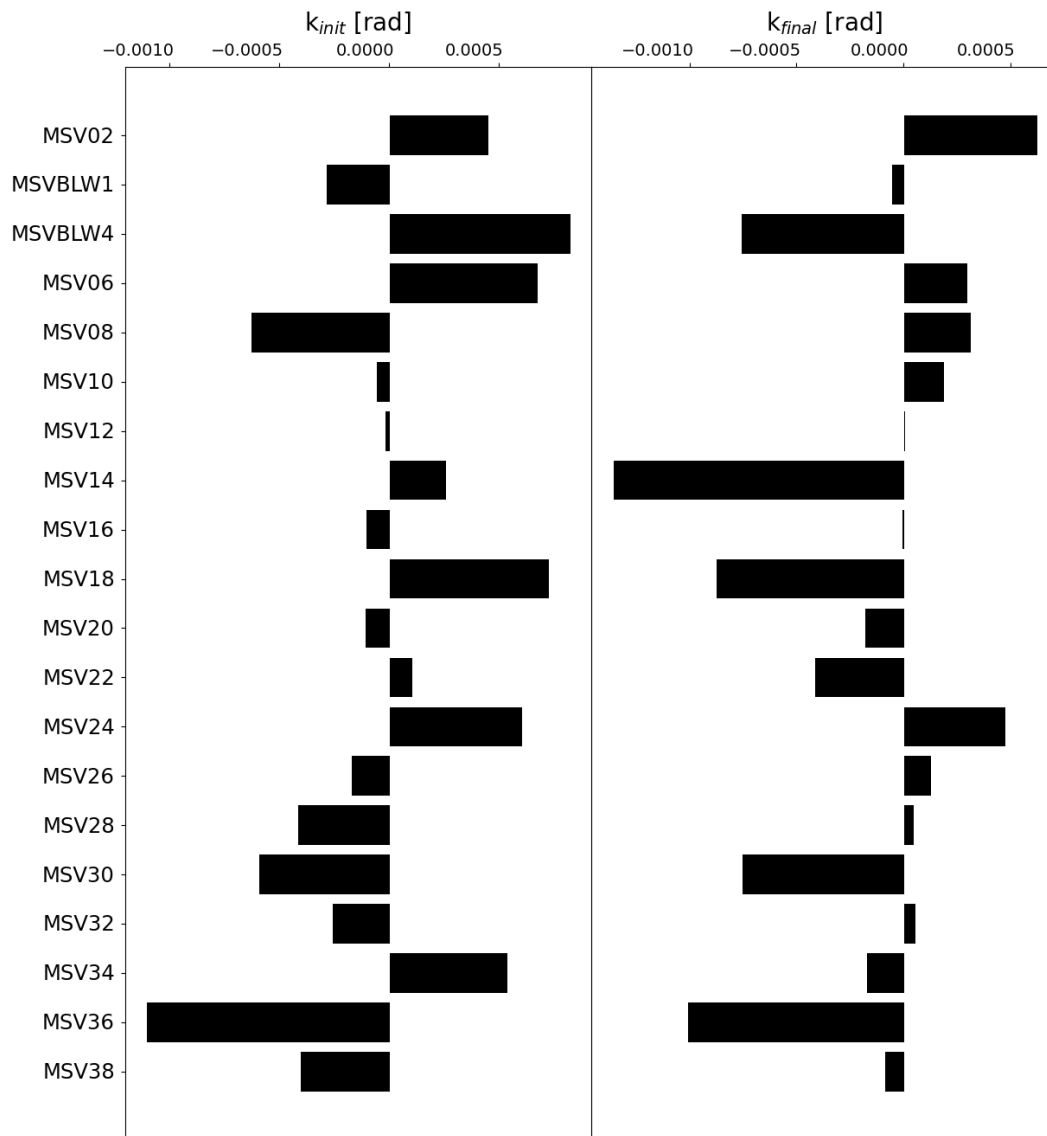


Figure 28: Vertical steerer settings used in the simulation. The plot on the left depicts the values of the initial random steerer settings used to distort the orbit. The plot on the right shows the values of the final vertical steerer values yielding the results shown in Figure 27.

6 Conclusion and Outlook

The JEDI collaboration at Forschungszentrum Jülich aims to directly measure the EDM of the fundamental particles for the first time. The high-precision experiments have been conducted with polarized deuterons, and a beam of polarized protons was first launched in February 2022. Investigating the EDM of various particles is of great importance for this kind of research, as only the direct measurements of several particles will provide information about the source of the \mathcal{CP} -violation.

Within this thesis, the modeling of an optical setting for the EDM measurements of protons at COSY has been performed. The purpose of the modeling was to implement the lattice of the storage ring and to discuss and study the systematic effects influencing the orbit of COSY. For correct implementation of the effects and thereby a valid description of the real facility, it was necessary to check whether the default model corresponds indeed to the theoretical predictions of the particle motion at all. Section 4.1 presents the results of benchmarking of the default model, which allowed quantifying the numerical limit of the model.

Next, magnet misalignments were investigated. As the simulation has shown, displacements and rotations of dipoles and quadrupoles represent one of the main distortion sources. The displacements and rotational errors measured by Vermessungsbüro Stollenwerk were included in the model. In addition, the phenomenon of dipole shortening was studied. Due to the close positioning of the surrounding magnets, the effective length of a dipole is influenced by the field of the surrounding magnets. The effect was shown on the simulated horizontal and vertical closed orbits. The estimates of the “kicks” included in the model were first deducted by H.J. Stein [59]. At this point, the new values have been calculated by M. Hartmann [60], which are only to be included in further simulations. Another study [51] demonstrated that the model describes the real orbit considerably better when the orbit correction is turned off and no correcting magnets are included in the simulation. In this case, the influence of the effective dipole lengths is even more noticeable. However, to study these interdependencies, further measurements without the orbit correction are required, which is rather challenging since the particles easily get lost. Further investigations of the magnetic fields should also involve quadrupoles, which fields are exposed to the influence of other

magnets as well.

Since the goal of modeling is to correctly describe a real accelerator, providing invaluable assistance in EDM experiments, the simulation model has to be of high quality and thus correspond to the obtained results as precisely as possible. To improve the simulation model, two algorithms were implemented into Bmad and applied to the measurements. One of the approaches lies in minimizing the difference between the simulated and measured orbit response matrices and thus allowing for a simultaneous fit of several parameters. However, this algorithm was not used to its full extent, since the ORM was not measured during the beam time with protons. Yet, it served as an instrument to describe the model, as well as to visualize the correlations between steerers and beam position monitors by evaluating the calculated matrix. The second method involves matching the simulated orbit to the measured orbit by changing the strengths of the correcting magnets. The combination of these two methods allows, in general, for a precise description of the experimental results, which has already been demonstrated in the course of this thesis. The final orbits, as seen in Section 5.3, have similarities not only in magnitude but even in some areas almost completely correspond to the orbit measured during the beam time.

Overall, the existing COSY simulation model has proven capable of describing measurements through the integration of additional systematic effects and implementation of a complex matching algorithm based on the calculation of an orbit response matrix. Despite its success in the context of this thesis, the model still requires improvements. Additional effects influencing the model accuracy, which were neglected this time, could be due to the effective lengths of quadrupoles, displacements of the BPMs, fringe fields, and effects of multipole components of magnets. An improved model with an underlying fitting procedure can optimize the data analysis, as well as facilitate the calculations and simulations before the next beam time.

References

- [1] A. D. Sakharov, “Violation of CP Invariance, C asymmetry, and baryon asymmetry of the universe,” *Zhurnal Eksperimental’noi i Teoreticheskoi Fiziki*, vol. 5, pp. 32–35, May 1967.
- [2] I. B. Khriplovich and S. K. Lamoreaux, *CP Violation Without Strangeness: Electric Dipole Moments of Particles, Atoms, and Molecules*. Springer Berlin, Heidelberg, 2011, ISBN: 9783540630944.
- [3] G. Guidoboni, “Spin Coherence Time Lengthening of a Polarized Deuteron Beam Using Sextupole Fields,” in *Proc. 6th International Particle Accelerator Conference (IPAC’15)*, JACoW, Jun. 2015, pp. 4066–4069. [Online]. Available: <http://jacow.org/ipac2015/papers/thpf146.pdf>.
- [4] G. Guidoboni *et al.*, “How to reach a thousand-second in-plane polarization lifetime with 0.97–GeV/ c deuterons in a storage ring,” *Physical Review Letters*, vol. 117, p. 054 801, 5 Jul. 2016. [Online]. Available: <https://link.aps.org/doi/10.1103/PhysRevLett.117.054801>.
- [5] J. Pretz, “Electric dipole moment measurements at storage rings,” *Journal of Physics: Conference Series*, vol. 1586, no. 1, p. 012 043, Aug. 2020. [Online]. Available: <https://doi.org/10.1088/1742-6596/1586/1/012043>.
- [6] D. Sagan, “Bmad: A relativistic charged particle simulation library,” *Nuclear Instruments and Methods in Physics Research Section A: Accelerators, Spectrometers, Detectors and Associated Equipment*, vol. A558, no. 1, pp. 356–359, 2006.
- [7] A. Wirzba, “Electric dipole moments of the nucleon and light nuclei,” *Nuclear Physics A*, vol. 928, pp. 116–127, Aug. 2014.
- [8] L. Canetti, M. Drewes, and M. Shaposhnikov, “Matter and antimatter in the universe,” *New Journal of Physics*, vol. 14, no. 9, p. 095 012, Sep. 2012.
- [9] Planck Collaboration *et al.*, “Planck 2013 results. XVI. cosmological parameters,” *Astronomy & Astrophysics*, vol. 571, A16, Oct. 2014.

- [10] W. Bernreuther, “CP Violation and Baryogenesis,” in *CP Violation in Particle, Nuclear, and Astrophysics*, M. Beyer, Ed., vol. 591, arXiv, 2002, pp. 237–293.
- [11] T. Fukuyama, “Searching for new physics beyond the standard model in electric dipole moment,” *International Journal of Modern Physics A*, vol. 27, no. 16, p. 1230015, Jun. 2012.
- [12] N. F. Ramsey and A. Weis, “Suche nach permanenten elektrischen dipolmomenten: Ein test der zeitumkehrinvarianz,” *Physikalische Blätter*, vol. 52, no. 9, pp. 859–863, 1996.
- [13] M. Rosenthal, “Experimental benchmarking of spin tracking algorithms for electric dipole moment searches at the Cooler Synchrotron COSY,” Ph.D. dissertation, RWTH Aachen University, 2016. [Online]. Available: <https://publications.rwth-aachen.de/record/671012>.
- [14] C. J. G. Onderwater, “Search for electric dipole moments at storage rings,” *Hyperfine Interactions*, vol. 211, no. 1-3, pp. 9–14, Feb. 2012.
- [15] C. Abel *et al.*, “Measurement of the permanent electric dipole moment of the neutron,” *Physical Review Letters*, vol. 124, no. 8, p. 081803, Feb. 2020.
- [16] The ACME Collaboration, J. Baron, W. C. Campbell, *et al.*, “Order of magnitude smaller limit on the electric dipole moment of the electron,” *Science*, vol. 343, no. 6168, pp. 269–272, Jan. 2014.
- [17] F. Rathmann and N. Nikolaev, “Precursor experiments to search for permanent electric dipole moments of protons and deuterons at COSY,” in *Proceedings of 8th International Conference on Nuclear Physics at Storage Rings — PoS(STOR11)*, vol. 150, 2012, p. 29.
- [18] H. Wiedemann, *Particle accelerator physics*, 4th ed. Berlin: Springer Cham, 2015, ISBN: 978-3-319-18317-6.
- [19] K. Wille and J. McFall, *The Physics of Particle Accelerators: An Introduction*. Oxford University Press, 2000, ISBN: 9780198505495.

- [20] F. Hinterberger, *Physik der Teilchenbeschleuniger und Ionenoptik*, 2nd ed. Berlin Heidelberg: Springer Berlin, Heidelberg, 2008, ISBN: 978-3-540-75282-0.
- [21] S. Y. Lee, *Accelerator Physics*, 2nd. World Scientific, 2004, ISBN: 978-981-256-200-5.
- [22] G. W. Hill, “On the part of the motion of the lunar perigee which is a function of the mean motions of the sun and moon,” *Acta Mathematica*, vol. 8, no. 1, pp. 1–36, 1886.
- [23] B. Holzer, “Transverse Beam Dynamics,” *CERN Yellow Rep. School Proc.*, vol. 5, pp. 1–30, 2018. [Online]. Available: <https://cds.cern.ch/record/2674115>.
- [24] R. Steinhagen, “Tune and chromaticity diagnostics,” *CAS 2008 - CERN Accelerator School: Beam Diagnostics, Proceedings*, pp. 317–359, Jan. 2009. [Online]. Available: <https://cds.cern.ch/record/1213281>.
- [25] B. Holzer, *Lattice design in high-energy particle accelerators*, 2014. [Online]. Available: <https://cds.cern.ch/record/1982419>.
- [26] P. Forck, P. Kowina, and D. Liakin, “Beam position monitors,” *CAS - CERN Accelerator School: Course on Beam Diagnostics, Dourdan, France*, pp. 187–228, Jun. 2008.
- [27] T. Wagner, “Beam-based alignment at the cooler synchrotron COSY for an electric dipole moment measurement of charged particles,” Ph.D. dissertation, RWTH Aachen University, 2021. [Online]. Available: <https://publications.rwth-aachen.de/record/825703/files/825703.pdf>.
- [28] F. Rathmann and N. N. Nikolaev, “Electric dipole moment searches using storage rings,” *Proceedings of 23rd International Spin Physics Symposium*, vol. SPIN2018, P. Lenisa, G. Ciullo, M. Contalbrigo, and L. Pappalardo, Eds., 2019.
- [29] A. Halama, C. Boehme, V. Kamerdzhev, F. Klehr, and S. Srinivasan, “Numerical comparative study of bpm designs for the HESR at FAIR,” Mar. 2017, pp. 608–611.
- [30] Ströher, Hans, “EDM experiments at storage rings,” *EPJ Web of Conferences*, vol. 181, p. 01 031, 2018.
- [31] F. Tecker, *Longitudinal beam dynamics*, 2014. [Online]. Available: <https://cds.cern.ch/record/1982417>.

- [32] J. Buon and J.-P. Koutchouk, “Polarization of electron and proton beams,” *Conf. Proc. C*, pp. 879–940, 1995.
- [33] G. H. Hoffstaetter, *High-Energy Polarized Proton Beams. A Modern View*. Springer New York, NY, Jan. 2006, vol. 218, ISBN: 978-0-387-34754-7.
- [34] S. Y. Lee, *Spin Dynamics and Snakes in Synchrotrons*. World Scientific, 1997, ISBN: 978-981-3105-01-0.
- [35] V. Bargmann, L. Michel, and V. L. Telegdi, “Precession of the polarization of particles moving in a homogeneous electromagnetic field,” *Physical Review Letters*, vol. 2, pp. 435–436, 10 May 1959.
- [36] L. H. Thomas, “I. The kinematics of an electron with an axis,” *The London, Edinburgh, and Dublin Philosophical Magazine and Journal of Science*, vol. 3, no. 13, pp. 1–22, 1927.
- [37] T. Fukuyama and A. J. Silenko, “Derivation of generalized thomas-bargmann-michel-telegdi equation for a particle with electric dipole moment,” *International Journal of Modern Physics A*, vol. 28, no. 29, p. 1 350 147, Nov. 2013.
- [38] B. Lorentz, R. Gebel, A. Lehrach, R. Maier, D. Prasuhn, and H. Stockhorst, “Status and future plans of polarized beams at COSY,” *Journal of Physics: Conference Series*, vol. 295, May 2011.
- [39] J. Pretz, “Measurement of permanent electric dipole moments of charged hadrons in storage rings,” *Hyperfine Interactions*, vol. 214, no. 1-3, pp. 111–117, Feb. 2013. [Online]. Available: <https://doi.org/10.1007/s10751-013-0799-4>.
- [40] F. J. M. Farley, K. Jungmann, J. P. Miller, *et al.*, “New method of measuring electric dipole moments in storage rings,” *Physical Review Letters*, vol. 93, p. 052 001, 5 Jul. 2004.
- [41] F. Rathmann, A. Saleev, and N. N. Nikolaev, “Search for electric dipole moments of light ions in storage rings,” *Physics of Particles and Nuclei*, vol. 45, no. 1, pp. 229–233, 2014. [Online]. Available: <https://doi.org/10.1134/S1063779614010869>.

- [42] R. Maier, “Cooler synchrotron COSY — performance and perspectives,” *Nuclear Instruments and Methods in Physics Research Section A: Accelerators, Spectrometers, Detectors and Associated Equipment*, vol. 390, no. 1, pp. 1–8, 1997.
- [43] J. Slim, “A novel waveguide RF Wien filter for electric dipole moment measurements of deuterons and protons at the COoler SYnchrotron (COSY)/Jülich,” Ph.D. dissertation, Rheinisch-Westfälische Technische Hochschule Aachen, 2018. [Online]. Available: <https://publications.rwth-aachen.de/record/748558/files/748558.pdf>.
- [44] H. Stein, D. Prasuhn, H. Stockhorst, *et al.*, “Current Status of the COSY Electron Cooler (Jülich, Germany),” *Atomic energy*, vol. 94, pp. 24–26, 2003.
- [45] R. Maier, U. Bechstedt, J. Dietrich, *et al.*, “Cooler synchrotron COSY,” *Nuclear Physics A*, vol. 626, no. 1, pp. 395–403, 1997, Proceedings of the Third International Conference on Nuclear Physics at Storage Rings.
- [46] D. Prasuhn, J. Dietrich, R. Maier, R. Stassen, H. Stein, and H. Stockhorst, “Electron and stochastic cooling at COSY,” *Nuclear Instruments and Methods in Physics Research Section A: Accelerators, Spectrometers, Detectors and Associated Equipment*, vol. 441, pp. 167–174, Feb. 2000.
- [47] H. Poth, “Electron cooling: Theory, experiment, application,” *Physics Reports*, vol. 196, no. 3, pp. 135–297, 1990.
- [48] D. Sagan, *The Bmad reference manual*, 2022. [Online]. Available: <https://www.classe.cornell.edu/bmad/manual.html>.
- [49] D. Sagan, *The Tao manual*, 2022. [Online]. Available: <https://www.classe.cornell.edu/bmad/tao.html>.
- [50] M. Clausen and L. Dalesio, “EPICS: Experimental physics and industrial control system,” *ICFA Beam Dyn. Newslett.*, vol. 47, pp. 56–66, 2008.
- [51] V. Poncza, “Extensive optimization of a simulation model for the electric dipole moment measurement at the Cooler Synchrotron COSY,” Ph.D. dissertation, RWTH

- Aachen University, 2021. [Online]. Available: <https://publications.rwth-aachen.de/record/819047/files/819047.pdf>.
- [52] Y. Cai, G. Bourianoff, B. Cole, *et al.*, “Decoupling Schemes for the SSC Collider,” *Conf. Proc. C*, vol. 930517, S. T. Corneliussen and L. Carlton, Eds., pp. 203–205, 1993.
- [53] S. Hacıömeroğlu and Y. K. Semertzidis, “Systematic errors related to quadrupole misplacement in an all-electric storage ring for proton EDM experiment,” *arXiv e-prints*, pp. 1–12, 2017.
- [54] V. Schmidt, “Analysis of Closed-Orbit Deviations for a first direct Deuteron Electric Dipole Moment Measurement at the Cooler Synchrotron COSY,” M.S. thesis, RWTH Aachen University, 2016. [Online]. Available: http://collaborations.fz-juelich.de/ikp/jedi/public_files/theses/thesis.pdf.
- [55] R. Holtzapfel, R. Eshelman, E. Egger, *et al.*, “Alignment of the Dipole Magnets in the Cornell Electron-Positron Storage Ring,” *Colliding Beam Notes*, 1998.
- [56] Vermessungsbüro Dipl.-Ing. H.J. Stollenwerk, Bahnstasse 8, 50126 Bergheim.
- [57] V. Schmidt and A. Lehrach, “Analysis of closed orbit deviations for a first direct deuteron electric dipole moment measurement at the cooler synchrotron COSY,” *Journal of Physics: Conference Series*, vol. 874, p. 012 051, Jul. 2017. [Online]. Available: <https://doi.org/10.1088/1742-6596/874/1/012051>.
- [58] L. Leunissen, “Non-linear transverse dynamics at the cooler synchrotron COSY,” Ph.D. dissertation, Applied Physics, 1997. [Online]. Available: <https://pure.tue.nl/ws/portalfiles/portal/3622994/9704806.pdf>.
- [59] H. Stein, Private communication, 2022.
- [60] M. Hartmann, Private communication, 2022.
- [61] G. H. Hoffstaetter, J. Keil, and A. Xiao, “Orbit-response matrix analysis at HERA,” in *8th European Particle Accelerator Conference (EPAC 2002)*, Jun. 2002, pp. 407–409.

- [62] Y. Chung, G. Decker, and K. Evans, “Closed orbit correction using singular value decomposition of the response matrix,” in *Proceedings of International Conference on Particle Accelerators*, 1993, pp. 2263–2265.
- [63] W. Press, S. Teukolsky, W. Vetterling, and B. Flannery, *Numerical Recipes 3rd Edition: The Art of Scientific Computing*. Cambridge University Press, 2007, ISBN: 978-0521880688.
- [64] F. Zimmermann, “Measurement and correction of accelerator optics,” in *Joint US-CERN-Japan-Russia School on Particle Accelerators: Beam Measurement*, Jun. 1998, pp. 21–107.
- [65] The University of Texas at Austin, *PLAPACK: Parallel linear algebra package*, 1997. [Online]. Available: <https://www.cs.utexas.edu/users/plapack>.
- [66] X. Huang, *Beam-based Correction and Optimization for Accelerators*. Dec. 2019, ISBN: 9780429434358.

A Phase Space Simulations

Longitudinal Momentum Offset

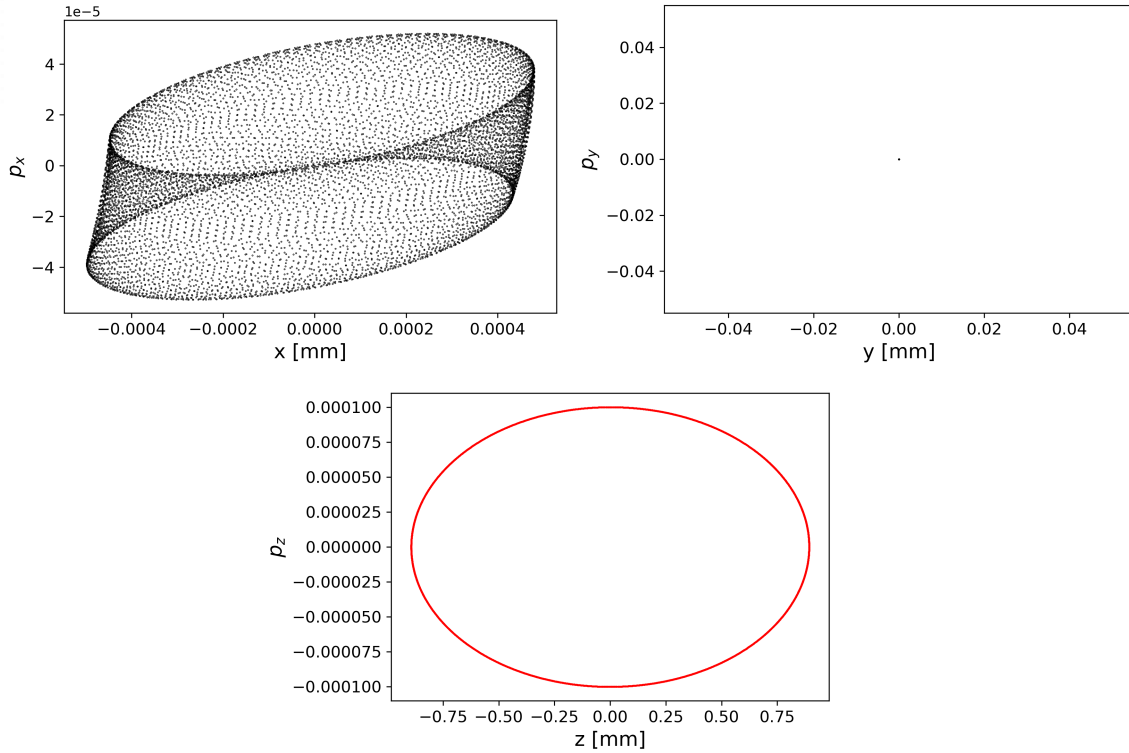


Figure 29: Three-dimensional phase space of a particle with a longitudinal momentum offset $\frac{\Delta p}{p_0}$. The shift in a longitudinal direction does not affect the vertical phase space. The horizontal motion is determined by the betatron oscillations.

B Magnet Misalignments

Dipole Rotations

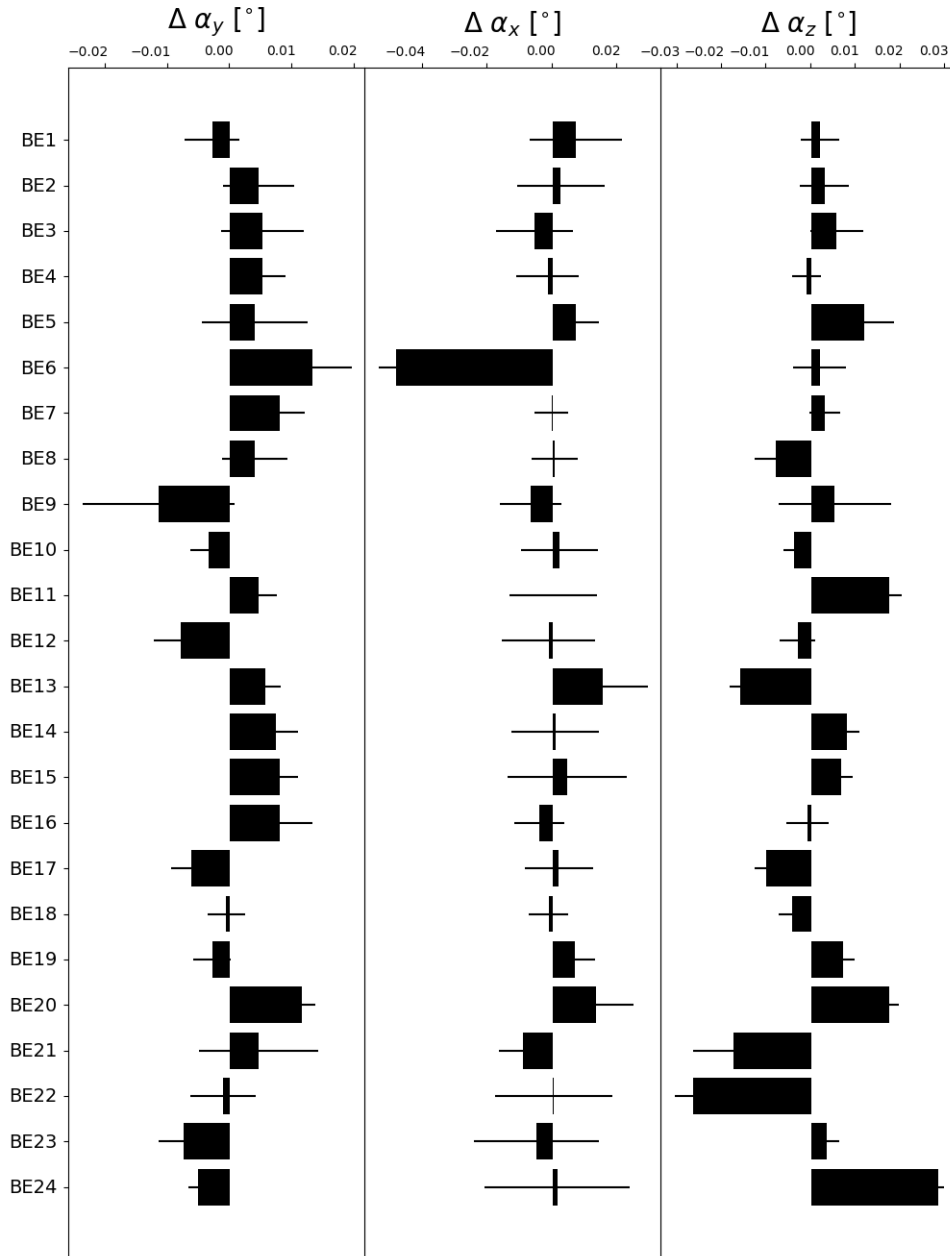


Figure 30: Rotation errors of the COSY dipoles including the measurement uncertainties. $\Delta\alpha_z$ gives a rotation around the z-, $\Delta\alpha_x$, and $\Delta\alpha_y$ around the x- and y-axes, respectively. The measurements were conducted in 2019 by Vermessungsbüro Stollenwerk [56].

Quadrupole Misalignments

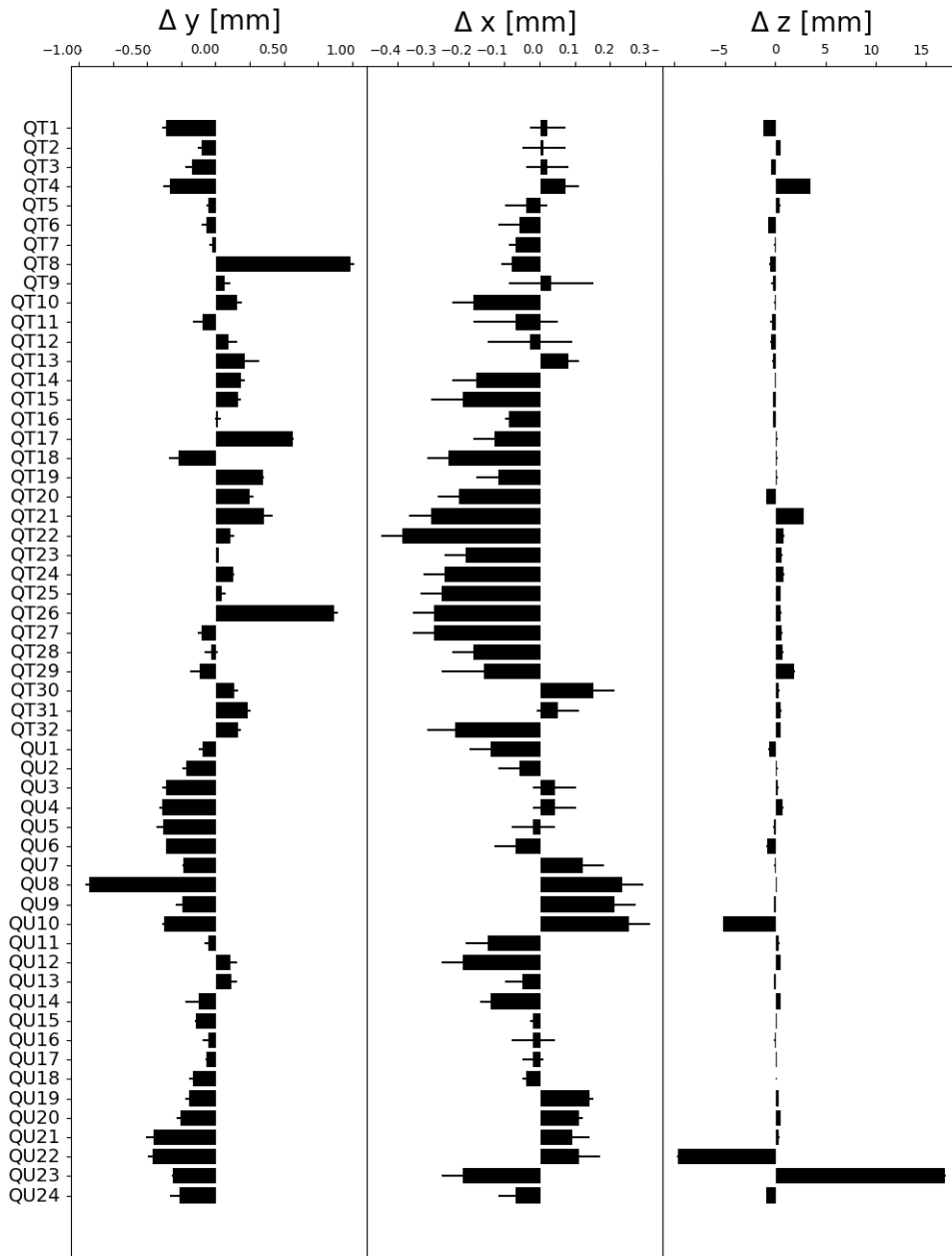


Figure 31: Mechanical misalignment of the COSY quadrupoles including the measurement uncertainties. Δz gives a displacement in a longitudinal, Δx and Δy in horizontal and vertical directions, respectively. The measurements were conducted in 2019 by Vermessungsbüro Stoltenwerk [56].

Quadrupole Rotations

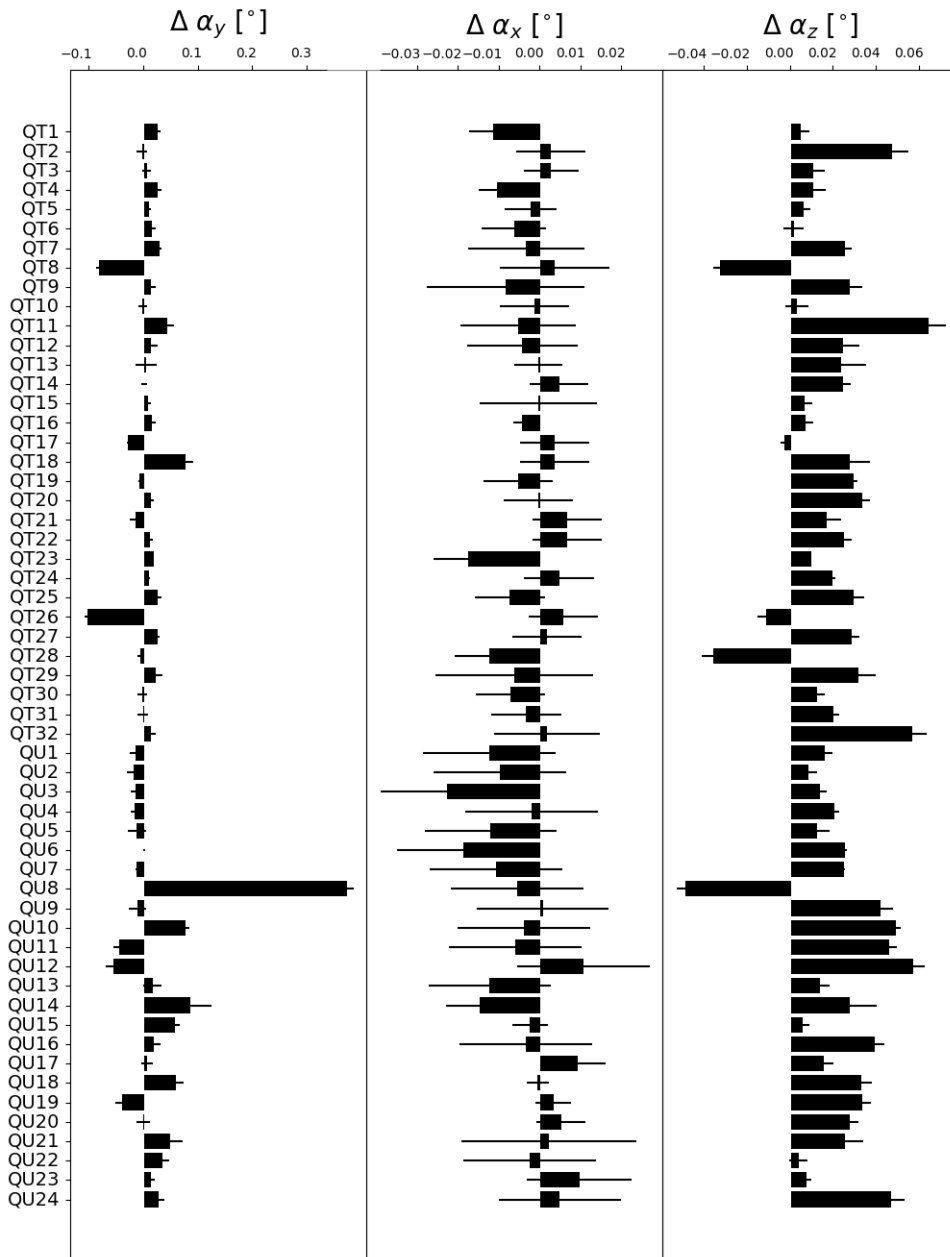


Figure 32: Rotation errors of the COSY quadrupoles including the measurement uncertainties. $\Delta\alpha_z$ gives a rotation around the z-, $\Delta\alpha_x$, and $\Delta\alpha_y$ around the x- and y-axes, respectively. The measurements were conducted in 2019 by Vermessungsbüro Stollenwerk [56].

C Results of Model Fitting

Horizontal Steerer Settings

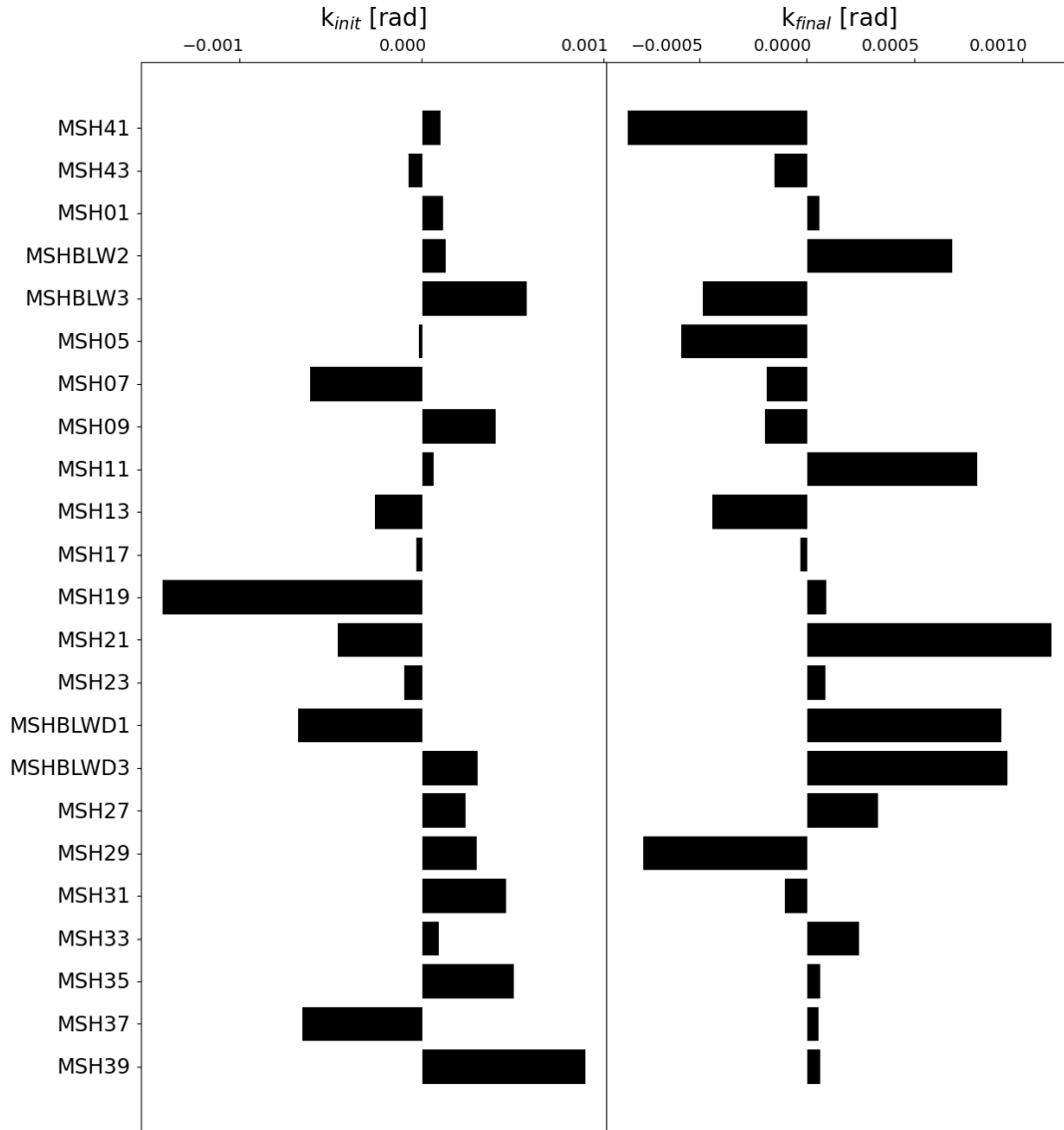


Figure 33: Horizontal steerer settings used in the simulation. The plot on the left depicts the values of the initial random steerer settings used to distort the orbit. The plot on the right shows the values of the final horizontal steerer values yielding the results shown in Figure 27.

List of Figures

1	Behaviour of the EDM and MDM under parity \mathcal{P} and time reversal \mathcal{T} transformations. Applying a parity transformation flips the sign of the electric field \vec{E} , while time reversal transformation flips $\vec{d}, \vec{\mu}$, and the sign of the magnetic field \vec{B} . Adapted from [13].	5
2	Co-moving Cartesian coordinate system $(\vec{e}_x, \vec{e}_y, \vec{e}_z)$ with its origin located at the position of reference particles. The initial position of a particle is depicted in black and the final position is in blue, whereas θ is an angle between them. .	6
3	Particle trajectory within a beam envelope $E(s)$. Its size is determined by a particle with the highest emittance value ϵ . Adapted from [19].	10
4	Phase space ellipse of particle motion for a horizontal phase space. The horizontal offset is given by a shift along the x-axis. The x'-axis gives a derivative of an offset. The optical functions α, γ , and β define the size and shape of an ellipse. The area of the ellipse A is defined by an emittance ϵ . Adapted from [19].	10
5	A schematic cross-section of a quadrupole magnet with magnetic field lines. The beam goes perpendicular to the x-y-plane. Adapted from [19].	12
6	Chromatic focusing errors caused by the variation of the focal length f of the quadrupole. This effect of momentum dependence is called chromaticity. The focusing quadrupole is represented by a focusing lens. Adapted from [18]. . . .	14
7	Chromaticity correction with sextupoles. Particles of higher energy are focused less and particles of lower energy than an ideal particle are focused more by a sextupole. Adapted from [18].	15
8	Schematic of a sextupole magnet with poles and equipotential lines. a is the distance from the center of a magnet to the pole. Adapted from [19].	15
9	Induced image current $I_{image}(t)$ on the beam pipe wall caused by the positively charged particle flux $I_{beam}(t)$. Adapted from [26].	16
10	Diagonal cut cylindrical BPM used in COSY. The horizontal and vertical positions of the beam are determined by the voltage differences of electrodes 1 and 2, and electrodes 3 and 4, respectively. Adapted from [28].	17
11	Energy gain as a function of particle phase. For $\gamma < \gamma_{tr}$ the rising flank is used for acceleration, for $\gamma > \gamma_{tr}$ the falling one. Adapted from [19].	20

12	Principle of a storage ring EDM measurement. An EDM tilts the spin \vec{s} in the vertical direction ($\vec{\Omega}_{EDM}$), while MDM causes the spin precession $\vec{\Omega}_{MDM}$ in the horizontal plane. Reprinted from [5].	23
13	Sketch of the COSY storage ring, the pre-accelerator JULIC, and the injection beamline. Reprinted from [43].	25
14	COSY lattice designed in TAO [49]. Lattice includes all of the elements present in the storage ring COSY. For better readability, only the bending magnets (BE1 – BE24) and the sextupoles (green) are labeled in the graph. The quadrupoles are marked in pink.	27
15	Optical functions β_x, β_y, D_x of the default lattice. The quadrupole settings are adjusted such that dispersion D_x is zero in the straight sections.	29
16	Transverse coordinates x and y describe the offset of an actual orbit from a reference orbit. Adapted from [48].	30
17	Closed orbit of a COSY lattice calculated using the <code>closed_orbit_calc</code> subroutine. The plots reveal the deviations of the horizontal, vertical, and longitudinal phase space coordinates (from top to bottom). The x-axis gives a position s on the ring.	31
18	Left column: three-dimensional phase space of a particle with a horizontal offset Δx . Due to the dispersive effects, various ellipses appear in the longitudinal phase space. Right column: three-dimensional phase space of a particle with a vertical offset Δy . The distortions in the horizontal phase space result from the non-vanishing dispersion in the arcs.	33
19	Reference marks P1 – P5 on top of the COSY dipoles (left) and quadrupoles (right). The red dashed line is the beam path. Adapted from [57].	34
20	Mechanical misalignment of the COSY dipoles including the measurement uncertainties. Δz gives a displacement in a longitudinal, Δx and Δy in horizontal and vertical directions, respectively. The measurements were conducted in 2019 by Vermessungsbüro Stollenwerk [56].	35
21	Horizontal x and vertical y closed orbits resulting from dipole shortening effect with an underlying ideal lattice (top) and including magnet misalignments (bottom).	36

22	Simulated and measured horizontal x and vertical y orbits. The simulation includes the same magnet settings used during the run in February – March 2022, as well as the changed effective dipole lengths and the magnet misalignments.	39
23	Orbit response matrix of an optical model. It is used to describe the accelerator and usually does not correspond with a measured ORM [61].	41
24	Evolution of the steerer kick values after 1, 3, and 5 iterations of the orbit matching procedure of a default model. The matching result improves after each iteration adjusting the kick values such that the orbit becomes less distorted. After the 5 th iteration the values of the steerers reach zero.	45
25	RMS values trend of the simulated orbits after each iteration of the orbit matching algorithm. The default orbit is distorted by the normally distributed steerer kicks. Benchmarking shows that after the 5 th iteration the RMS values of the closed orbits are reduced by more than 7 orders of magnitude.	46
26	RMS values trend of the horizontal and vertical orbits after each iteration of the orbit matching algorithm. The RMS values of both orbits approach the measured RMS values after the 2 nd iteration and remain roughly constant after the 3 rd one.	47
27	Results of the orbit matching procedure. The simulated horizontal and vertical orbits resemble the measured ones already after the 3 rd iteration. The steerer magnet values used to obtain this result are presented in Figures 28 and 33.	48
28	Vertical steerer settings used in the simulation. The plot on the left depicts the values of the initial random steerer settings used to distort the orbit. The plot on the right shows the values of the final vertical steerer values yielding the results shown in Figure 27.	50
29	Three-dimensional phase space of a particle with a longitudinal momentum offset $\frac{\Delta p}{p_0}$. The shift in a longitudinal direction does not affect the vertical phase space. The horizontal motion is determined by the betatron oscillations.	61
30	Rotation errors of the COSY dipoles including the measurement uncertainties. $\Delta\alpha_z$ gives a rotation around the z-, $\Delta\alpha_x$, and $\Delta\alpha_y$ around the x- and y-axes, respectively. The measurements were conducted in 2019 by Vermessungsbüro Stollenwerk [56].	62

31 Mechanical misalignment of the COSY quadrupoles including the measurement uncertainties. Δz gives a displacement in a longitudinal, Δx and Δy in horizontal and vertical directions, respectively. The measurements were conducted in 2019 by Vermessungsbüro Stollenwerk [56]. 63

32 Rotation errors of the COSY quadrupoles including the measurement uncertainties. $\Delta\alpha_z$ gives a rotation around the z-, $\Delta\alpha_x$, and $\Delta\alpha_y$ around the x- and y-axes, respectively. The measurements were conducted in 2019 by Vermessungsbüro Stollenwerk [56]. 64

33 Horizontal steerer settings used in the simulation. The plot on the left depicts the values of the initial random steerer settings used to distort the orbit. The plot on the right shows the values of the final horizontal steerer values yielding the results shown in Figure 27. 65

List of Tables

1	Measured upper limits of EDM searches.	5
2	Measured values of the gyromagnetic anomaly G of the particles. Taken from [38].	22
3	Effective lengths of magnets at COSY. Quadrupoles in arcs and quadrupoles in straight sections have different lengths, as well as all three sextupole types. Taken from [51].	28
4	Simulated and measured betatron tunes Q_x and Q_y for the same magnet settings.	38
5	Results of the benchmarking of the <code>y_orbit_match</code> subroutine for the first five steerers with an initial MSV02 kick value $k = -0.1$ mrad. Values of the other steerer magnets are set to 0.	44

Eidesstaatliche Erklärung

Name, Vorname

Matrikelnummer

Ich versichere hiermit an Eides Statt, dass ich die vorliegende Masterarbeit mit dem Titel **Modeling of the Optical Setting for the Measurement of the Electric Dipole Moment of Protons at Cooler Synchrotron COSY** selbstständig und ohne unzulässige fremde Hilfe (insbes. akademisches Ghostwriting) erbracht habe. Ich habe keine anderen als die angegebenen Quellen und Hilfsmittel benutzt. Für den Fall, dass die Arbeit zusätzlich auf einem Datenträger eingereicht wird, erkläre ich, dass die schriftliche und die elektronische Form vollständig übereinstimmen. Die Arbeit hat in gleicher oder ähnlicher Form noch keiner Prüfungsbehörde vorgelegen.

Ort, Datum

Unterschrift